AD-A121 026 VISCOUS FLOWFIELDS INDUCED BY THREE-DIMENSIONAL LIFT JETS IN GROUND EFFECT(U) MCDONNELL DOUGLAS RESEARCH LABS ST LOUIS MO W W BOWER 30 JAN 82 MDC-Q0769 1/1

UNCLASSIFIED N00014-80-C-0454 F/G 20/4 NL

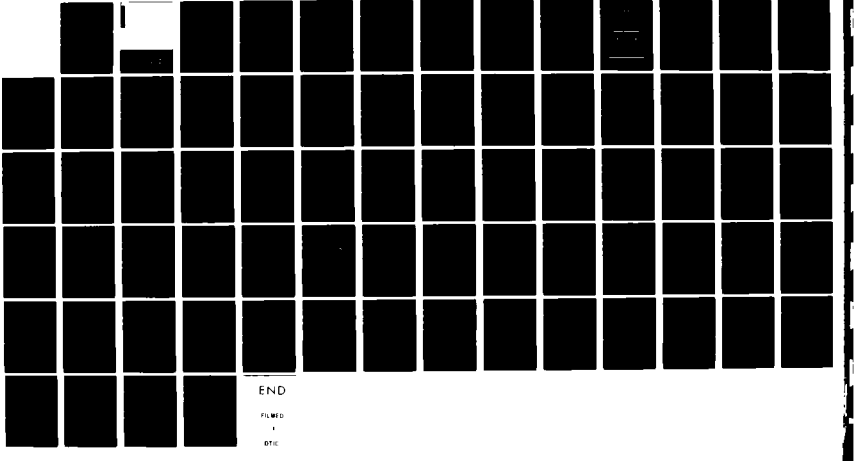

END

FILMED

DTIC

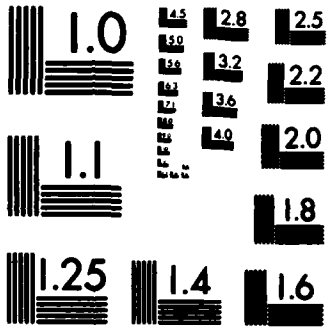

MICROCOPY RESOLUTION TEST CHART
NATIONAL BUREAU OF STANDARDS-1963-A

MCDONNELL DOUGLAS RESEARCH LABORATORIES

MCDONNELL DOUGLAS CORPORATION

DTIC
ELECTE
NOV 3 1982
S D

DTIC FILE COPY

82 11 03 001

UNCLASSIFIED

SECURITY CLASSIFICATION OF THIS PAGE *(When Data Entered)*

REPORT DOCUMENTATION PAGE		READ INSTRUCTIONS BEFORE COMPLETING FORM
1. REPORT NUMBER	2. GOVT ACCESSION NO. AD-A121 026	3. RECIPIENT'S CATALOG NUMBER
4. TITLE *(and Subtitle)* VISCOUS FLOWFIELDS INDUCED BY THREE-DIMENSIONAL LIFT JETS IN GROUND EFFECT		5. TYPE OF REPORT & PERIOD COVERED Final Technical Report 22 Sep 80 - 30 Nov 81
		6. PERFORMING ORG. REPORT NUMBER
7. AUTHOR(s) W. W. Bower		8. CONTRACT OR GRANT NUMBER(s) N00014-80-C-0454
9. PERFORMING ORGANIZATION NAME AND ADDRESS McDonnell Douglas Research Laboratories McDonnell Douglas Corporation P.O. Box 516, St. Louis, MO 63166		10. PROGRAM ELEMENT, PROJECT, TASK AREA & WORK UNIT NUMBERS
11. CONTROLLING OFFICE NAME AND ADDRESS Office of Naval Research Mathematical and Information Sciences Division, Code 211, 800 N. Quincy St., Arlington, VA 22217		12. REPORT DATE 1 December 1981
		13. NUMBER OF PAGES 72
14. MONITORING AGENCY NAME & ADDRESS(if different from Controlling Office)		15. SECURITY CLASS. (of this report) Unclassified
		15a. DECLASSIFICATION/DOWNGRADING SCHEDULE

16. DISTRIBUTION STATEMENT *(of this Report)*

Approved for public release; distribution unlimited.

17. DISTRIBUTION STATEMENT *(of the abstract entered in Block 20, if different from Report)*

18. SUPPLEMENTARY NOTES

19. KEY WORDS *(Continue on reverse side if necessary and identify by block number)*

VTOL lift jet
Ground effect
Viscous
Turbulence modeling
Finite-difference methods

20. ABSTRACT *(Continue on reverse side if necessary and identify by block number)*

The turbulent flowfields associated with single and multiple jets impinging on a ground plane are relevant to the aerodynamics of VTOL aircraft in ground effect. These flowfields are computed using the Reynolds equations and a two-equation turbulence model to describe an isolated jet and two interacting jets with fountain formation. Coordinate transformations are employed to apply the boundary conditions for the governing equations in the far field, and a third-

DD FORM 1 JAN 73 1473 EDITION OF 1 NOV 65 IS OBSOLETE

UNCLASSIFIED

SECURITY CLASSIFICATION OF THIS PAGE *(When Data Entered)*

order-accurate upwind-difference scheme is used to discretize the resulting system. Flowfield properties calculated for these impinging-jet configurations are presented and compared with experimental data.

PREFACE

This final technical report documents the work completed at the McDonnell Douglas Research Laboratories (MDRL) on Viscous Flowfields Induced by Three-Dimensional Lift Jets in Ground Effect, Contract No. N00014-80-C-0454, from 22 September 1980 to 30 January 1982. The principal investigator was Dr. W. W. Bower. The program monitor was Dr. R. E. Whitehead, Office of Naval Research (ONR), Arlington, VA.

Accession For	
NTIS GRA&I	X
DTIC TAB	☐
Unannounced	☐
Justification	
By	
Distribution/	
Availability Codes	
Dist	Avail and/or Special
A	

CONTENTS

		Page
1.	INTRODUCTION	1
2.	THE FLOWFIELD MODEL	6
	2.1 Governing Equations	6
	2.2 Coordinate Transformations	11
	2.3 Boundary Conditions	13
3.	THE NUMERICAL SOLUTION SCHEME	16
	3.1 Discretization of the Poisson-Type Equations	16
	3.2 Discretization of the Transport-Type Equations	20
	3.3 Discretization of the Boundary Conditions	25
	3.4 Solution of the Coupled System of Equations	29
4.	THE COMPUTED FLOWFIELDS	32
	4.1 Laminar Channel Flow	32
	4.2 Turbulent Isolated Jet-Impingement Flow	34
	4.3 Turbulent Interacting Jet-Impingement Flow	47
5.	SUMMARY	58
REFERENCES		61
DISTRIBUTION LIST		63

LIST OF ILLUSTRATIONS

Figure		Page
1	Schematic illustration in planar view of three-dimensional impinging-jet configurations	2
2	Streamline plots for equal- and unequal-strength jets with normal impingement ($Re = V_{jce2}D_2/\nu = 100$)	4
3	The three-dimensional finite-difference stencil	16
4	Computing sequence used in the solution of the flowfield equations	30
5	Velocity profiles for laminar channel flow (Re = 75)	33
6	Flow properties for an isolated jet with normal impingement	37
7	Flow properties for an isolated jet with normal impingement	39
8	Flow properties for an isolated jet with inclined impingement	40
9	Flow properties for an isolated jet with inclined impingement	43
10	Flow properties for an isolated jet with normal impingement in the presence of a blocking plate	45
11	Flow properties for equal-strength jets with normal impingement (S/D = 6, H/D = 3, Re = 200)	50
12	Flow properties for equal-strength jets with normal impingement (S/D = 6, H/D = 3, Re = 200)	51
13	Flow properties for equal-strength jets with normal impingement (S/D = 12, H/D = 4, Re = 100)	53
14	Computational domain for unequal-strength jets with normal impingement in the presence of a blocking plate	54
15	Flow properties for unequal-strength jets with normal impingement ($S/D_1 = 6$, $H/D_1 = 2$, $D_2/D_1 = 0.75$, Re = 100)	56
16	Flow properties for unequal-strength jets with normal impingement ($S/D_1 = 6$, $H/D_1 = 2$, $D_2/D_1 = 0.515$, Re = 100)	57

LIST OF TABLES

Table		Page
1	Coefficients in the discretized form of the transport equation.....	24

1. INTRODUCTION

Because of their relevance to the aerodynamics of vertical-takeoff-and-landing aircraft in ground effect, considerable research has recently been devoted to isolated and interacting impinging jets. Figure 1 illustrates these configurations schematically in planar view. For the case of a single jet, Figure 1(a), there are four simultaneous flow regimes of differing character: the transition region in which the jet velocity profile changes from a uniform to a fully developed distribution; the fully developed region; the impingement region in which the fluid is deflected by the ground plane; and the wall-jet region in which the flow spreads radially from the stagnation point. For the case of two interacting jets, Figure 1(b), these four regimes exist for each of the impinging jets, and, in addition, a fountain region is formed through the collision of the opposing wall jets.

Although the flow patterns illustrated in Figure 1 appear simple, they are nevertheless difficult to compute because they are characterized by significant turbulence levels, strong pressure gradients, and an elliptic character which precludes analysis by parabolic marching schemes. The ground-plane pressure distribution in the impingement zone, which is governed by the dynamics of the flow, can be predicted adequately by inviscid analytical methods, but calculation of entrainment effects and velocity profiles in the wall jet and fountain necessitates the inclusion of turbulence.

For isolated impinging jets, both two- and three-dimensional, Rubel has solved the conservation equations for inviscid flow in finite-difference form, References 1 and 2. These analyses provided good agreement between measured and computed ground-plane pressure distributions for both normal and oblique impingement. For two-dimensional (planar) impinging jets, Agarwal and Bower, Reference 3, included viscous effects by solving the time-averaged Navier-Stokes equations for both incompressible and compressible flow and using the two-equation Jones-Launder model to obtain closure. This work yielded good agreement with pressure and velocity data and provided information on the variation of turbulence length scale with Reynolds number.

For two interacting, impinging jets with fountain formation, most techniques developed to predict these flows use the so-called "modular analyses,"

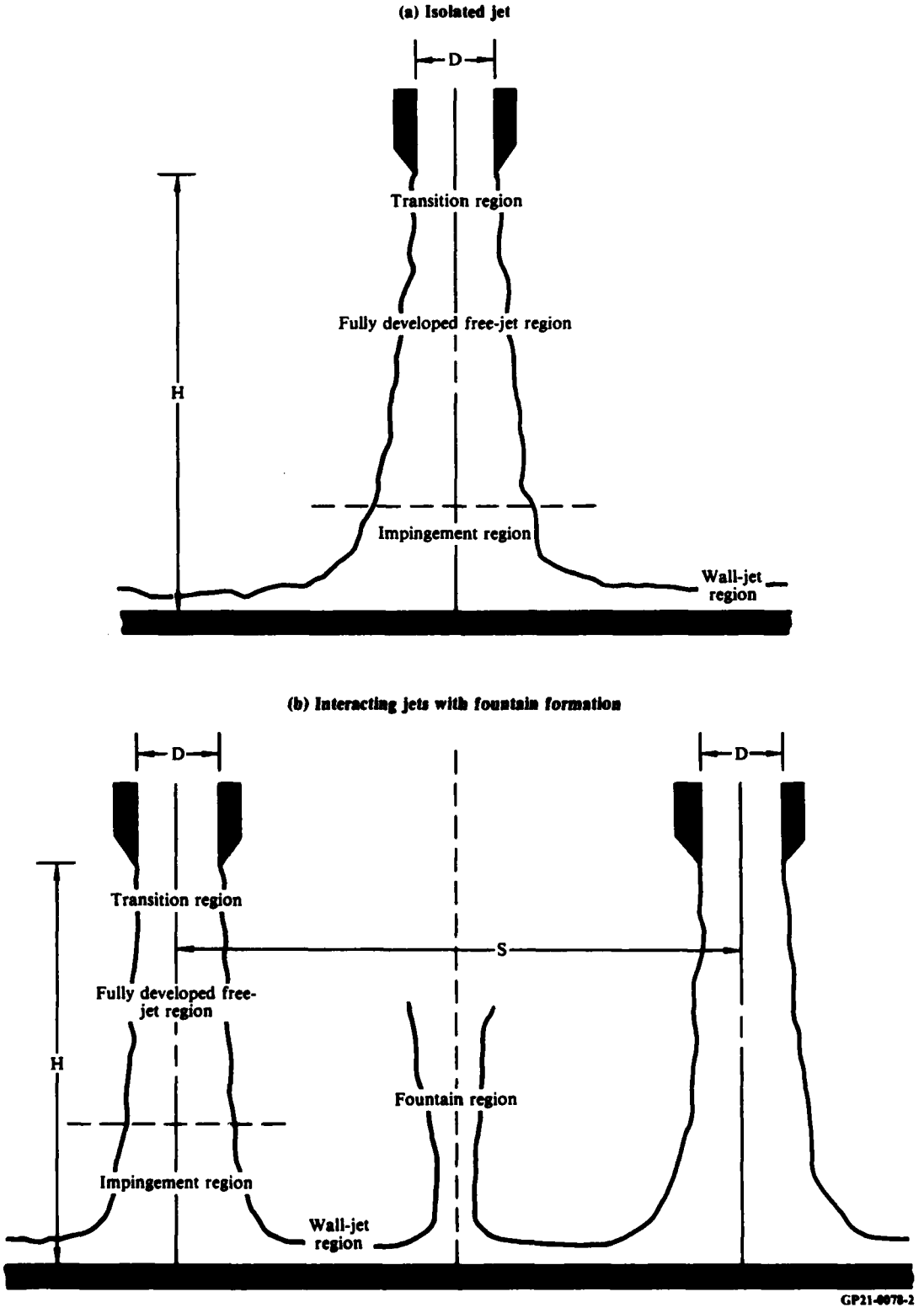

Figure 1. Schematic illustration in planar view of three-dimensional impinging-jet configurations.

such as those described by Kotansky et al., Reference 4, and Siclari et al., Reference 5. With this approach, the various regions of the flowfield, such as the free jets and the wall jet, are modeled using a separate system of equations for each zone, which are generally based on integral conservation-law constraints. The computed properties are then iteratively pieced together to provide the quantities of interest. This method works well for relatively wide jet spacing (S/D > 6) where the fountain properties are dependent primarily on the properties of the approaching wall jets. However, as S/D is reduced below 6, there is a strong interaction between the impinging jets and the fountain, as established in the flow visualization work of Saripalli, Reference 6. The coupling between the primary jets and the fountain invalidates any prediction model that computes the upwash based only on the wall-jet properties. Siclari et al., Reference 7, have formulated a "modular analysis" for closely spaced jets, but this scheme is restricted by the need for numerous empirical constants which are configuration-dependent.

A more general approach for computing dual-jet impingement flows is the solution of the time-averaged Navier-Stokes equations in three dimensions. This problem is considerably more complex than the planar impinging-jet problem for the following two reasons:

(1) Computer storage limitations restrict the number of finite-difference grid points available, which limits the maximum Reynolds number for which convergent or accurate solutions can be obtained.

(2) Even with coarse grids, the computer time necessary to achieve a three-dimensional solution is at least an order of magnitude greater than the time necessary to compute a two-dimensional solution, which translates directly into cost considerations.

Initial work at MDRL on solution of the three-dimensional, time-averaged, Navier-Stokes equations was based on writing the conservation equations in terms of scalar and vector potential functions and vorticity, using the one-equation Glushko model to represent the turbulence, applying experimentally determined boundary conditions in the near field, and solving the transport equations using Hoffman's augmented-central-difference algorithm (Reference 8). With this approach, flowfields were computed for equal- and unequal-strength jets with normal and oblique impingement, and representative results given in the form of particle pathline traces are illustrated in Figure 2.

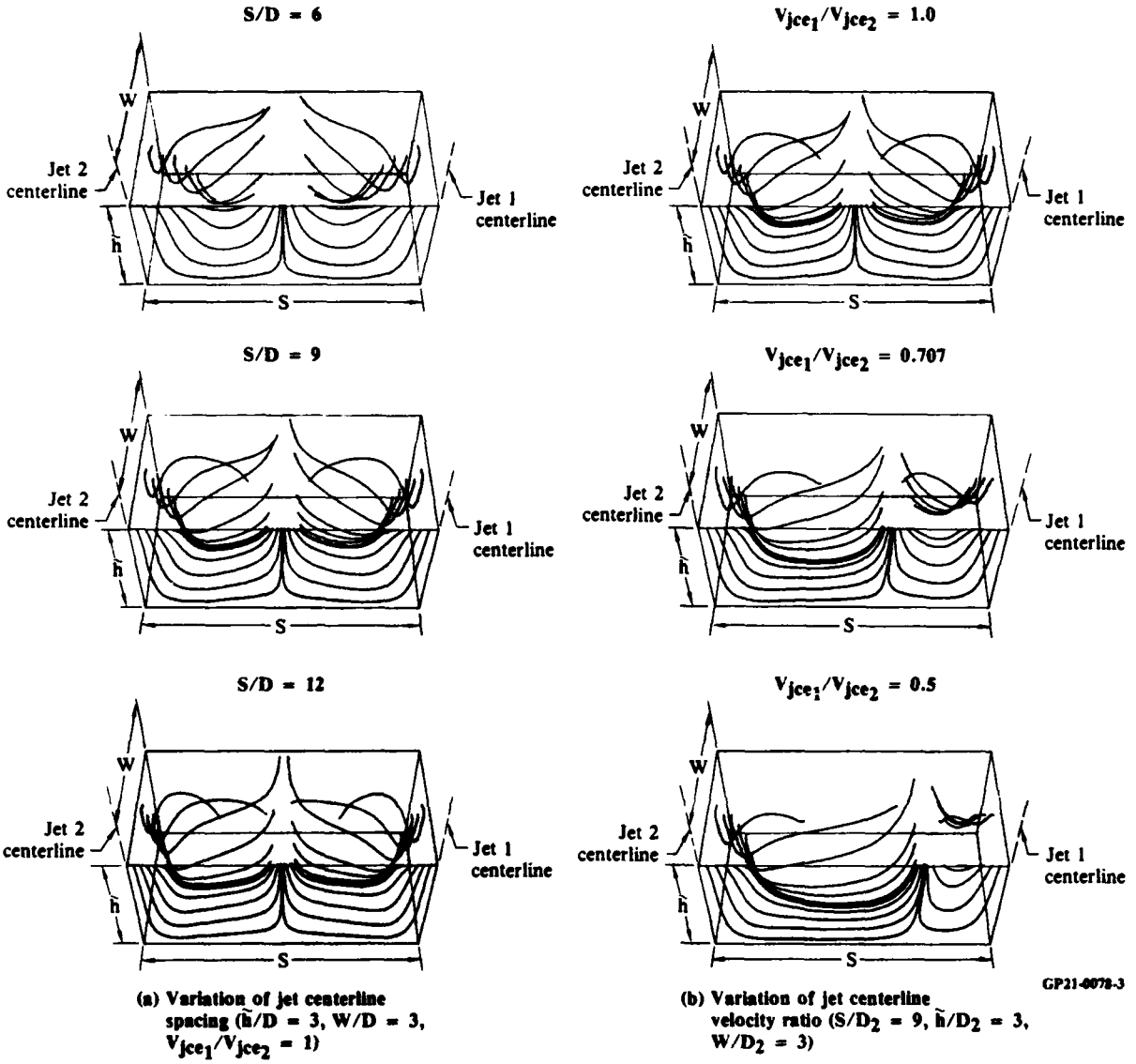

(a) Variation of jet centerline spacing ($\tilde{h}/D$ = 3, W/D = 3, V_{jce_1}/V_{jce_2} = 1)

(b) Variation of jet centerline velocity ratio (S/D_2 = 9, $\tilde{h}/D_2$ = 3, W/D_2 = 3)

Figure 2. Streamline plots for equal- and unequal-strength jets with normal impingement ($Re = V_{jce_2}D_2/\mu$ = 100).

Shortcomings of this formulation are the need to specify in the Glushko model the length-scale distribution of the turbulence, which is a complex variation for jet-impingement flows, and the need to establish the boundary conditions in the near field, which generally must be evaluated from experimental results. To overcome these limitations, the following are the specific objectives of the current work on solution of the time-averaged Navier-Stokes equations for three-dimensional turbulent impinging-jet flows:

(1) Utilize the Jones-Launder, two-equation turbulence model, thereby eliminating the need to specify the length-scale distribution.

(2) Utilize coordinate transformations which permit imposing the boundary conditions in the far field where relatively simple constraints can be placed on the flow variables, thereby eliminating the need to introduce empirically based boundary conditions in the near field.

(3) Solve the governing equations directly for the velocity and vorticity, thereby eliminating the need for scalar and vector potential functions which require additional computer storage.

(4) Discretize the transport-type equations using a third-order-accurate upwind-difference scheme which is more efficient than the augmented central-difference algorithm.

This report describes the governing equations, the numerical solution technique, and computed jet-impingement flowfields. The latter include isolated jets with both normal and oblique impingement and interacting equal- and unequal-strength jets with fountain formation.

2. THE FLOWFIELD MODEL

This section presents the governing equations used to describe the turbulent, incompressible, steady flow of the three-dimensional impinging-jet configurations. The complete time-averaged Navier-Stokes equations and Jones-Launder turbulence model equations are given first in terms of the velocity components and pressure, and then they are rewritten in terms of velocity and vorticity. Coordinate transformations are applied to the equations, and the types of boundary conditions imposed in the analysis are defined.

2.1 Governing Equations

Considering a space-fixed reference through which the fluid moves, the time-averaged continuity and momentum (Navier-Stokes) equations for steady incompressible flow are given below in tensor notation.

Conservation of mass:

$$\frac{\partial \bar{u}_j}{\partial x_j} = 0 \tag{1}$$

Conservation of momentum in the i^{th} direction:

$$\rho \frac{\partial (\bar{u}_j \bar{u}_i)}{\partial x_j} + \frac{\partial \bar{p}}{\partial x_i} - \frac{\partial}{\partial x_j} (\bar{\tau}_{ij} - \rho \overline{u_i' u_j'}) = 0 \tag{2}$$

The conventional notation is used in which ρ is the density, u_i the velocity component in the i^{th} direction, p the static pressure, and τ_{ij} the shear stress in the i^{th} direction on a surface normal to the j^{th} direction.

The previous equations were derived using Reynolds decomposition in which a general flow variable ϕ is expressed as the sum of a time-averaged component $\bar{\phi}$ and a fluctuating component ϕ', $\phi = \bar{\phi} + \phi'$. The result is a system of time-averaged conservation equations which have the same form as the instantaneous conservation equations with the exception of the Reynolds stress term $- \rho \overline{u_i' u_j'}$.

In order to obtain a closed system of equations, the Reynolds stress term must be related to the time-averaged quantities that describe the mean flow.

The present work uses the high-Reynolds-number form of the two-equation Jones-Launder (k-ε) turbulence model, Reference 9. With this approach, the effective shear-stress term in Equation (2) is represented by

$$\bar{\tau}_{ij} - \rho\overline{u_i' u_j'} = \mu_{eff} \left(\frac{\partial \bar{u}_i}{\partial x_j} + \frac{\partial \bar{u}_j}{\partial x_i} \right) - \frac{2}{3} \delta_{ij} \rho k, \tag{3}$$

where μ_{eff} is the effective viscosity (the sum of the molecular and turbulent components, $\mu_{eff} = \mu + \mu_t$) and k is the turbulent kinetic energy. In the high-Reynolds-number form of the Jones-Launder turbulence model, μ_t is related to the turbulent kinetic energy k and its kinematic rate of dissipation ε by

$$\mu_t = \frac{c_\mu \rho k^2}{\varepsilon}, \tag{4}$$

where c_μ is a constant with a value of 0.09. In this turbulence model, k and ε are computed from the transport equations given below in tensor notation.

Transport equation for turbulent kinetic energy:

$$\rho \bar{u}_j \frac{\partial k}{\partial x_j} = \frac{\partial}{\partial x_j} \left(\mu_k \frac{\partial k}{\partial x_j} \right) + \mu_t \left(\frac{\partial \bar{u}_i}{\partial x_j} + \frac{\partial \bar{u}_j}{\partial x_i} \right) \frac{\partial \bar{u}_i}{\partial x_j} - \rho\varepsilon \tag{5}$$

Transport equation for turbulent dissipation:

$$\rho \bar{u}_j \frac{\partial \varepsilon}{\partial x_j} = \frac{\partial}{\partial x_j} \left(\mu_\varepsilon \frac{\partial \varepsilon}{\partial x_j} \right) + \frac{C_1 \varepsilon}{k} \mu_t \left(\frac{\partial \bar{u}_i}{\partial x_j} + \frac{\partial \bar{u}_j}{\partial x_i} \right) \frac{\partial \bar{u}_i}{\partial x_j} - \frac{C_2 \rho \varepsilon^2}{k} \tag{6}$$

In Equations (5) and (6) the diffusion coefficients μ_k and μ_ε are defined by

$$\mu_k = \mu + \lambda_k \mu_t \tag{7}$$

and

$$\mu_\varepsilon = \mu + \lambda_\varepsilon \mu_t. \tag{8}$$

The constants appearing in the turbulence-model transport equations have the following values: $C_1 = 1.44$, $C_2 = 1.92$, $\lambda_k = 1.0$, and $\lambda_\varepsilon = 0.9091$.

Although the governing equations are written in velocity-pressure form, they are solved in velocity-vorticity form to simplify the solution procedure by eliminating the pressure gradient from the momentum equations. The vorticity is defined in tensor notation by

$$\Omega_i = \epsilon_{ijk} \frac{\partial u_k}{\partial x_j} , \tag{9}$$

where ϵ_{ijk} is the alternating tensor. Taking the curl of Equation (2) and utilizing Equation (9) results in a transport equation for the vorticity. A Poisson equation for the velocity field is derived by combining the relation for the conservation of mass, Equation (1), with Equation (9).

Completing the steps outlined in the previous paragraph, introducing a characteristic length D and characteristic velocity V_o to normalize the equations, and expanding the equations in cartesian coordinates (x,y,z) with velocity components (u,v,w) and vorticity components $(\Omega_x,\Omega_y,\Omega_z)$ results in the system of dimensionless equations given below.

Poisson equation for u:

$$\frac{\partial^2 u}{\partial x^2} + \frac{\partial^2 u}{\partial y^2} + \frac{\partial^2 u}{\partial z^2} = \frac{\partial \Omega_y}{\partial z} - \frac{\partial \Omega_z}{\partial y} \tag{10}$$

Poisson equation for v:

$$\frac{\partial^2 v}{\partial x^2} + \frac{\partial^2 v}{\partial y^2} + \frac{\partial^2 v}{\partial z^2} = \frac{\partial \Omega_z}{\partial x} - \frac{\partial \Omega_x}{\partial z} \tag{11}$$

Poisson equation for w:

$$\frac{\partial^2 w}{\partial x^2} + \frac{\partial^2 w}{\partial y^2} + \frac{\partial^2 w}{\partial z^2} = \frac{\partial \Omega_x}{\partial y} - \frac{\partial \Omega_y}{\partial x} \tag{12}$$

Transport equation for Ω_x:

$$(1 + \mathrm{Re}\ \mu_t)\left(\frac{\partial^2\Omega_x}{\partial x^2} + \frac{\partial^2\Omega_x}{\partial y^2} + \frac{\partial^2\Omega_x}{\partial z^2}\right) + \mathrm{Re}\left(2\frac{\partial\mu_t}{\partial x} - u\right)\frac{\partial\Omega_x}{\partial x}$$

$$+ \mathrm{Re}\left(2\frac{\partial\mu_t}{\partial y} - v\right)\frac{\partial\Omega_x}{\partial y} + \mathrm{Re}\left(2\frac{\partial\mu_t}{\partial z} - w\right)\frac{\partial\Omega_x}{\partial z}$$

$$= \mathrm{Re}\left[-\frac{\partial u}{\partial x}\Omega_x - \frac{\partial u}{\partial y}\Omega_y - \frac{\partial u}{\partial z}\Omega_z + \frac{\partial\mu_t}{\partial x}\frac{\partial\Omega_x}{\partial x}\right.$$

$$+ \frac{\partial\mu_t}{\partial y}\frac{\partial\Omega_y}{\partial x} + \frac{\partial\mu_t}{\partial z}\frac{\partial\Omega_z}{\partial x} - \frac{\partial^2\mu_t}{\partial x\partial y}\left(\frac{\partial w}{\partial x} + \frac{\partial u}{\partial z}\right)$$

$$- 2\frac{\partial^2\mu_t}{\partial y\partial z}\left(\frac{\partial w}{\partial z} - \frac{\partial v}{\partial y}\right) - \frac{\partial^2\mu_t}{\partial y^2}\left(\frac{\partial w}{\partial y} + \frac{\partial v}{\partial z}\right)$$

$$\left. + \frac{\partial^2\mu_t}{\partial x\partial z}\left(\frac{\partial v}{\partial x} + \frac{\partial u}{\partial y}\right) + \frac{\partial^2\mu_t}{\partial z^2}\left(\frac{\partial v}{\partial z} + \frac{\partial w}{\partial y}\right)\right] \qquad (13)$$

Transport equation for Ω_y:

$$(1 + \mathrm{Re}\ \mu_t)\left(\frac{\partial^2\Omega_y}{\partial x^2} + \frac{\partial^2\Omega_y}{\partial y^2} + \frac{\partial^2\Omega_y}{\partial z^2}\right) + \mathrm{Re}\left(2\frac{\partial\mu_t}{\partial x} - u\right)\frac{\partial\Omega_y}{\partial x}$$

$$+ \mathrm{Re}\left(2\frac{\partial\mu_t}{\partial y} - v\right)\frac{\partial\Omega_y}{\partial y} + \mathrm{Re}\left(2\frac{\partial\mu_t}{\partial z} - w\right)\frac{\partial\Omega_y}{\partial z}$$

$$= \mathrm{Re}\left[-\frac{\partial v}{\partial x}\Omega_x - \frac{\partial v}{\partial y}\Omega_y - \frac{\partial v}{\partial z}\Omega_z + \frac{\partial\mu_t}{\partial x}\frac{\partial\Omega_x}{\partial y}\right.$$

$$+ \frac{\partial\mu_t}{\partial y}\frac{\partial\Omega_y}{\partial y} + \frac{\partial\mu_t}{\partial z}\frac{\partial\Omega_z}{\partial y} + \frac{\partial^2\mu_t}{\partial x\partial y}\left(\frac{\partial w}{\partial y} + \frac{\partial v}{\partial z}\right)$$

$$- \frac{\partial^2\mu_t}{\partial y\partial z}\left(\frac{\partial u}{\partial y} + \frac{\partial v}{\partial x}\right) + \frac{\partial^2\mu_t}{\partial x^2}\left(\frac{\partial w}{\partial x} + \frac{\partial u}{\partial z}\right)$$

$$\left. - 2\frac{\partial^2\mu_t}{\partial x\partial z}\left(\frac{\partial u}{\partial x} - \frac{\partial w}{\partial z}\right) - \frac{\partial^2\mu_t}{\partial z^2}\left(\frac{\partial u}{\partial z} + \frac{\partial w}{\partial x}\right)\right] \qquad (14)$$

Transport equation for Ω_z:

$$(1 + Re\ \mu_t)\left(\frac{\partial^2\Omega_z}{\partial x^2} + \frac{\partial^2\Omega_z}{\partial y^2} + \frac{\partial^2\Omega_z}{\partial z^2}\right) + Re\ \left(2\frac{\partial\mu_t}{\partial x} - u\right)\frac{\partial\Omega_z}{\partial x}$$

$$+ Re\ \left(2\frac{\partial\mu_t}{\partial y} - v\right)\frac{\partial\Omega_z}{\partial y} + Re\ \left(2\frac{\partial\mu_t}{\partial z} - w\right)\frac{\partial\Omega_z}{\partial z}$$

$$= Re\ \left[-\frac{\partial w}{\partial x}\Omega_x - \frac{\partial w}{\partial y}\Omega_y - \frac{\partial w}{\partial z}\Omega_z + \frac{\partial\mu_t}{\partial x}\frac{\partial\Omega_x}{\partial z}\right.$$

$$+ \frac{\partial\mu_t}{\partial y}\frac{\partial\Omega_y}{\partial z} + \frac{\partial\mu_t}{\partial z}\frac{\partial\Omega_z}{\partial z} - \frac{\partial^2\mu_t}{\partial x^2}\left(\frac{\partial v}{\partial x} + \frac{\partial u}{\partial y}\right)$$

$$- 2\frac{\partial^2\mu_t}{\partial x\partial y}\left(\frac{\partial v}{\partial y} - \frac{\partial u}{\partial x}\right) - \frac{\partial^2\mu_t}{\partial x\partial z}\left(\frac{\partial v}{\partial z} + \frac{\partial w}{\partial y}\right)$$

$$\left. + \frac{\partial^2\mu_t}{\partial y^2}\left(\frac{\partial u}{\partial y} + \frac{\partial v}{\partial x}\right) + \frac{\partial^2\mu_t}{\partial y\partial z}\left(\frac{\partial u}{\partial z} + \frac{\partial w}{\partial x}\right)\right] \qquad (15)$$

Transport equation for k:

$$(1 + \lambda_k\ Re\ \mu_t)\left(\frac{\partial^2 k}{\partial x^2} + \frac{\partial^2 k}{\partial y^2} + \frac{\partial^2 k}{\partial z^2}\right) + Re\ \left(\lambda_k\frac{\partial\mu_t}{\partial x} - u\right)\frac{\partial k}{\partial x}$$

$$+ Re\ \left(\lambda_k\frac{\partial\mu_t}{\partial y} - v\right)\frac{\partial k}{\partial y} + Re\ \left(\lambda_k\frac{\partial\mu_t}{\partial z} - w\right)\frac{\partial k}{\partial z}$$

$$= Re\ \varepsilon - Re\ \mu_t\left[2\frac{\partial u}{\partial x}\frac{\partial u}{\partial x} + \left(\frac{\partial u}{\partial y} + \frac{\partial v}{\partial x}\right)\frac{\partial u}{\partial y} + \left(\frac{\partial u}{\partial z} + \frac{\partial w}{\partial x}\right)\frac{\partial u}{\partial z}\right.$$

$$+ \left(\frac{\partial v}{\partial x} + \frac{\partial u}{\partial y}\right)\frac{\partial v}{\partial x} + 2\frac{\partial v}{\partial y}\frac{\partial v}{\partial y} + \left(\frac{\partial v}{\partial z} + \frac{\partial w}{\partial y}\right)\frac{\partial v}{\partial z}$$

$$\left. + \left(\frac{\partial w}{\partial x} + \frac{\partial u}{\partial z}\right)\frac{\partial w}{\partial x} + \left(\frac{\partial w}{\partial y} + \frac{\partial v}{\partial z}\right)\frac{\partial w}{\partial y} + 2\frac{\partial w}{\partial z}\frac{\partial w}{\partial z}\right] \qquad (16)$$

Transport equation for ε:

$$(1 + \lambda_\varepsilon \, Re \, \mu_t) \left(\frac{\partial^2 \varepsilon}{\partial x^2} + \frac{\partial^2 \varepsilon}{\partial y^2} + \frac{\partial^2 \varepsilon}{\partial z^2} \right) + Re \left(\lambda_\varepsilon \frac{\partial \mu_t}{\partial x} - u \right) \frac{\partial \varepsilon}{\partial x}$$

$$+ Re \left(\lambda_\varepsilon \frac{\partial \mu_t}{\partial y} - v \right) \frac{\partial \varepsilon}{\partial y} + Re \left(\lambda_\varepsilon \frac{\partial \mu_t}{\partial z} - w \right) \frac{\partial \varepsilon}{\partial z}$$

$$= \frac{Re \, C_2 \varepsilon^2}{k} - \frac{Re \, C_1 \varepsilon \mu_t}{k} \left[2 \frac{\partial u}{\partial x} \frac{\partial u}{\partial x} + \left(\frac{\partial u}{\partial y} + \frac{\partial v}{\partial x} \right) \frac{\partial u}{\partial y} \right.$$

$$+ \left(\frac{\partial u}{\partial z} + \frac{\partial w}{\partial x} \right) \frac{\partial u}{\partial z} + \left(\frac{\partial v}{\partial x} + \frac{\partial u}{\partial y} \right) \frac{\partial v}{\partial x} + 2 \frac{\partial v}{\partial y} \frac{\partial v}{\partial y}$$

$$+ \left(\frac{\partial v}{\partial z} + \frac{\partial w}{\partial y} \right) \frac{\partial v}{\partial z} + \left(\frac{\partial w}{\partial x} + \frac{\partial u}{\partial z} \right) \frac{\partial w}{\partial x} + \left(\frac{\partial w}{\partial y} + \frac{\partial v}{\partial z} \right) \frac{\partial w}{\partial y}$$

$$\left. + 2 \frac{\partial w}{\partial z} \frac{\partial w}{\partial z} \right] \qquad (17)$$

The only dimensionless parameter that enters the system of equations is the Reynolds number, $Re = V_o D/\nu$. The location in the flowfield where V_o and D are chosen will be defined subsequently with reference to the specific impinging-jet configurations.

2.2 Coordinate Transformations

In the present analysis, a transformation is used in each of the three coordinate directions. This approach permits mapping a relatively restricted computational domain into a larger physical domain and distributing points in the finite-difference solution of the equations in regions of the flowfield where property gradients are the largest.

The transformed coordinates are denoted by an overbar: $\bar{x} = \bar{x}(x)$, $\bar{y} = \bar{y}(y)$, and $\bar{z} = \bar{z}(z)$. It follows that the required derivatives of a general flow variable ϕ with respect to the physical coordinates are related to the derivatives with respect to the transformed coordinates by the expressions given below.

$$\frac{\partial \phi}{\partial x} = \frac{d\bar{x}}{dx} \frac{\partial \phi}{\partial \bar{x}} \tag{18}$$

$$\frac{\partial^2 \phi}{\partial x^2} = \left(\frac{d\bar{x}}{dx}\right)^2 \frac{\partial^2 \phi}{\partial \bar{x}^2} + \frac{d^2\bar{x}}{dx^2} \frac{\partial \phi}{\partial \bar{x}} \tag{19}$$

$$\frac{\partial \phi}{\partial y} = \frac{d\bar{y}}{dy} \frac{\partial \phi}{\partial \bar{y}} \tag{20}$$

$$\frac{\partial^2 \phi}{\partial y^2} = \left(\frac{d\bar{y}}{dy}\right)^2 \frac{\partial^2 \phi}{\partial \bar{y}^2} + \frac{d^2\bar{y}}{dy^2} \frac{\partial \phi}{\partial \bar{y}} \tag{21}$$

$$\frac{\partial \phi}{\partial z} = \frac{d\bar{z}}{dz} \frac{\partial \phi}{\partial \bar{z}} \tag{22}$$

$$\frac{\partial^2 \phi}{\partial z^2} = \left(\frac{d\bar{z}}{dz}\right)^2 \frac{\partial^2 \phi}{\partial \bar{z}^2} + \frac{d^2\bar{z}}{dz^2} \frac{\partial \phi}{\partial \bar{z}} \tag{23}$$

The Poisson equations for the velocity components, Equations (10) through (12), can be written in the following general form in terms of the physical coordinates:

$$\frac{\partial^2 \phi}{\partial x^2} + \frac{\partial^2 \phi}{\partial y^2} + \frac{\partial^2 \phi}{\partial z^2} = \sigma_\phi \ , \tag{24}$$

where ϕ = u, v, or w and σ_ϕ denotes the corresponding source term. In terms of the transformed coordinates, Equation (24) assumes the following form:

$$\alpha_1^2 \frac{\partial^2 \phi}{\partial \bar{x}^2} + \alpha_2 \frac{\partial \phi}{\partial \bar{x}} + \beta_1^2 \frac{\partial^2 \phi}{\partial \bar{y}^2} + \beta_2 \frac{\partial \phi}{\partial \bar{y}} + \gamma_1^2 \frac{\partial^2 \phi}{\partial \bar{z}^2} + \gamma_2 \frac{\partial \phi}{\partial \bar{z}} = \bar{\sigma}_\phi \ , \tag{25}$$

where

$$\alpha_1 = \frac{d\bar{x}}{dx} \ , \ \alpha_2 = \frac{d^2\bar{x}}{dx^2} \ , \ \beta_1 = \frac{d\bar{y}}{dy} \ , \ \beta_2 = \frac{d^2\bar{y}}{dy^2} \ , \ \gamma_1 = \frac{d\bar{z}}{dz} \ , \text{ and } \gamma_2 = \frac{d^2\bar{z}}{dz^2} \ .$$

The overbar on the source term σ_ϕ denotes that the derivatives it contains have been rewritten in terms of the transformed coordinates according to Equations (18) through (23).

Similarly, the transport equations for the vorticity components and the turbulence quantities, Equations (13) through (17), can be written in terms of the physical coordinates in the following general form:

$$\alpha_\phi \left(\frac{\partial^2 \phi}{\partial x^2} + \frac{\partial^2 \phi}{\partial y^2} + \frac{\partial^2 \phi}{\partial z^2} \right) + \beta_\phi \frac{\partial \phi}{\partial x} + \gamma_\phi \frac{\partial \phi}{\partial y} + \delta_\phi \frac{\partial \phi}{\partial z} = \sigma_\phi \ , \tag{26}$$

where $\phi = \Omega_x$, Ω_y, Ω_z, k, or ε. The corresponding coefficients in the respective equations are denoted by α_ϕ, β_ϕ, γ_ϕ, and δ_ϕ, and the source term is denoted by σ_ϕ. When Equation (26) is written in terms of the transformed coordinates, the following equation results:

$$\alpha_\phi \alpha_1^2 \frac{\partial^2 \phi}{\partial \bar{x}^2} + \alpha_\phi \beta_1^2 \frac{\partial^2 \phi}{\partial \bar{y}^2} + \alpha_\phi \gamma_1^2 \frac{\partial^2 \phi}{\partial \bar{z}^2} + \left(\alpha_\phi \alpha_2 + \beta_\phi \alpha_1 \right) \frac{\partial \phi}{\partial \bar{x}}$$

$$+ \left(\alpha_\phi \beta_2 + \gamma_\phi \beta_1 \right) \frac{\partial \phi}{\partial \bar{y}} + \left(\alpha_\phi \gamma_2 + \delta_\phi \gamma_1 \right) \frac{\partial \phi}{\partial \bar{z}} = \bar{\sigma}_\phi \ , \tag{27}$$

where α_1, α_2, β_1, β_2, γ_1, and γ_2 maintain the same definitions introduced with reference to Equation (25).

The analytic functions used to define the coordinate transformation derivatives are different for the various impinging-jet configurations considered and are defined in a subsequent section.

2.3 Boundary Conditions

In the system of equations presented in Section 2.1, the eight elliptic partial-differential equations must be solved for the following eight flow properties: u, v, w, Ω_x, Ω_y, Ω_z, k, and ε. The manner in which the boundary conditions are imposed on these equations depends on the nature of the boundary plane in the physical domain where the impinging-jet flowfield is solved.

Consider first the inflow plane where one or two jets enter the solution domain a distance $y = \tilde{h}$ above the ground. The velocity and turbulence property profiles throughout the entering jets are assumed to be known:

$$u = u(x, \tilde{h}, z),\ v = v(x, \tilde{h}, z),\ w = w(x, \tilde{h}, z),\ k = k(x, \tilde{h}, z),$$
$$\text{and } \varepsilon = \varepsilon(x, \tilde{h}, z). \tag{28}$$

The profiles of the vorticity components through the entering jet follow from the specified velocity distributions and the defining equations for the vorticity components,

$$\Omega_x = \frac{\partial w}{\partial y} - \frac{\partial v}{\partial z} \tag{29}$$

$$\Omega_y = \frac{\partial u}{\partial z} - \frac{\partial w}{\partial x} \tag{30}$$

$$\Omega_z = \frac{\partial v}{\partial x} - \frac{\partial u}{\partial y}\ . \tag{31}$$

On a solid surface (either the impingement plane or the blocking plate through which the jet discharges), the velocity and turbulent-kinetic-energy boundary values follow from the no-slip, impermeable-wall condition,

$$u = v = w = k = 0. \tag{32}$$

The turbulent dissipation is specified by taking the limiting form of Equation (16) at the wall,

$$\varepsilon = \frac{1}{Re} \frac{\partial^2 k}{\partial n^2}\ , \tag{33}$$

where n denotes the coordinate normal to the surface. The vorticity profiles follow from Equations (29) through (31).

On an outflow plane where the wall jet exits the solution domain, it is assumed that there are no gradients with respect to the coordinate normal to the outflow surface. (The outflow planes are taken sufficiently far from the impinging jet centerline such that this assumption is valid.)

$$\frac{\partial u}{\partial n} = \frac{\partial v}{\partial n} = \frac{\partial w}{\partial n} = \frac{\partial \Omega_x}{\partial n} = \frac{\partial \Omega_y}{\partial n} = \frac{\partial \Omega_z}{\partial n} = \frac{\partial k}{\partial n} = \frac{\partial \varepsilon}{\partial n} = 0\ . \tag{34}$$

Finally, the remaining boundary surface to consider is a symmetry plane passing through the impinging jet or fountain. On this plane the normal

velocity component vanishes, and the derivatives of the other velocity components with respect to the normal coordinate are zero.

$$u_n = 0, \quad \left.\frac{\partial u_i}{\partial n}\right|_{i \neq n} = 0 \ . \tag{35}$$

The normal gradients of the turbulence quantities vanish on the symmetry plane,

$$\frac{\partial k}{\partial n} = \frac{\partial \varepsilon}{\partial n} = 0 \ , \tag{36}$$

and the vorticity values follow from their defining equations.

Specific solution domains for the impinging-jet geometries and the corresponding boundary conditions are presented in Section 4.

3. THE NUMERICAL SOLUTION SCHEME

This section is a discussion of the finite-difference technique used to solve the partial-differential equations that describe the flowfield. The Poisson-type equations are discretized using the standard central-difference algorithm, and the transport-type equations are discretized using a third-order-accurate upwind-difference scheme. The discretization of the boundary conditions and the iterative solution of the coupled system of equations are described.

3.1 Discretization of the Poisson-Type Equations

As given in Section 2, the Poisson equations for the velocity components can be written in the form

$$\alpha_1^2 \frac{\partial^2 \phi}{\partial \bar{x}^2} + \alpha_2 \frac{\partial \phi}{\partial \bar{x}} + \beta_1^2 \frac{\partial^2 \phi}{\partial \bar{y}^2} + \beta_2 \frac{\partial \phi}{\partial \bar{y}} + \gamma_1^2 \frac{\partial^2 \phi}{\partial \bar{z}^2} + \gamma_2 \frac{\partial \phi}{\partial \bar{z}} = \bar{\sigma}_\phi, \tag{37}$$

where ϕ = u, v, or w.

To write Equation (37) in finite-difference form, the three-dimensional nodal network shown in Figure 3 is introduced. Since coordinate transformations are applied to the differential equations, a nonuniform finite-difference grid is not required to distribute nodes in regions of large

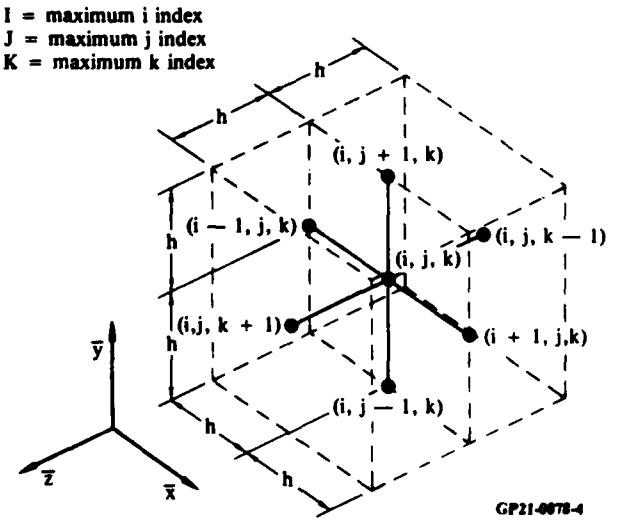

Figure 3. The three-dimensional finite-difference stencil.

property gradients. Consequently, a uniform grid spacing h is used in each of the transformed coordinate directions so that $\bar{x} = h(i - 2)$, $\bar{y} = h(j - 2)$, and $\bar{z} = h(k - 2)$, where i, j, and k are the respective node indices. The boundaries of the computational domain are the planes $i = 2$, $j = 2$, $k = 2$, $i = I$, $j = J$, and $k = K$; the planes $i = 1$, $j = 1$, $k = 1$, $i = I + 1$, $j = J + 1$, and $k = K + 1$ are exterior planes required in discretization of the transport-type equations.

The conventional central-difference algorithm is introduced with the derivatives centered at the interior point (i,j,k). The approximations for the first derivatives are

$$\left.\frac{\partial \phi}{\partial \bar{x}}\right|_{i,j,k} = \frac{\phi_{i+1,j,k} - \phi_{i-1,j,k}}{2h} \tag{38}$$

$$\left.\frac{\partial \phi}{\partial \bar{y}}\right|_{i,j,k} = \frac{\phi_{i,j+1,k} - \phi_{i,j-1,k}}{2h} \tag{39}$$

$$\left.\frac{\partial \phi}{\partial \bar{z}}\right|_{i,j,k} = \frac{\phi_{i,j,k+1} - \phi_{i,j,k-1}}{2h}, \tag{40}$$

and the approximations for the second derivatives are

$$\left.\frac{\partial^2 \phi}{\partial \bar{x}^2}\right|_{i,j,k} = \frac{\phi_{i+1,j,k} - 2\phi_{i,j,k} + \phi_{i-1,j,k}}{h^2} \tag{41}$$

$$\left.\frac{\partial^2 \phi}{\partial \bar{y}^2}\right|_{i,j,k} = \frac{\phi_{i,j+1,k} - 2\phi_{i,j,k} + \phi_{i,j-1,k}}{h^2} \tag{42}$$

$$\left.\frac{\partial^2 \phi}{\partial \bar{z}^2}\right|_{i,j,k} = \frac{\phi_{i,j,k+1} - 2\phi_{i,j,k} + \phi_{i,j,k-1}}{h^2}. \tag{43}$$

When Equations (38) through (43) are substituted into Equation (37), the discretized form of the Poisson equation is

$$P_1\phi_{i+1,j,k} + P_3\phi_{i-1,j,k} + P_4\phi_{i,j+1,k} + P_5\phi_{i,j-1,k} + P_6\phi_{i,j,k+1}$$

$$+ P_7\phi_{i,j,k-1} + P_2\phi_{i,j,k} = P_8. \tag{44}$$

The coefficients are defined by the following relations:

$$P_1 = \alpha_1^2 + 0.5h\alpha_2 \tag{45}$$

$$P_3 = \alpha_1^2 - 0.5h\alpha_2 \tag{46}$$

$$P_4 = \beta_1^2 + 0.5h\beta_2 \tag{47}$$

$$P_5 = \beta_1^2 - 0.5h\beta_2 \tag{48}$$

$$P_6 = \gamma_1^2 + 0.5h\gamma_2 \tag{49}$$

$$P_7 = \gamma_1^2 - 0.5h\gamma_2 \tag{50}$$

$$P_2 = -2(\alpha_1^2 + \beta_1^2 + \gamma_1^2) \tag{51}$$

$$P_8 = h^2\bar{\sigma}_\phi. \tag{52}$$

To solve the system of algebraic finite-difference equations, Equation (44) is rewritten for $3 < j < J - 1$ in the following form:

$$P_4\phi_{i,j+1,k} + P_2\phi_{i,j,k} + P_5\phi_{i,j-1,k} = P_8 - P_1\phi_{i+1,j,k}$$

$$- P_3\phi_{i-1,j,k} - P_6\phi_{i,j,k+1} - P_7\phi_{i,j,k-1}. \tag{53}$$

Applying Equation (44) for $j = 3$, $\phi_{i,2,k}$ is known from the boundary value and is transferred to the right side of the equation. Therefore,

$$P_4\phi_{i,4,k} + P_2\phi_{i,3,k} = P_8 - P_1\phi_{i+1,3,k} - P_3\phi_{i-1,3,k} - P_5\phi_{i,2,k}$$

$$- P_6\phi_{i,3,k+1} - P_7\phi_{i,3,k-1}. \tag{54}$$

Similarly, when Equation (44) is written for $j = J - 1$, $\phi_{i,J,k}$ is known from the boundary value and is transferred to the right side of the equation.

$$P_2\phi_{i,J-1,k} + P_5\phi_{i,J-2,k} = P_8 - P_1\phi_{i+1,J-1,k} - P_3\phi_{i-1,J-1,k} - P_4\phi_{i,J,k} - P_6\phi_{i,J-1,k+1} - P_7\phi_{i,J-1,k-1} \quad (55)$$

Equations (53) through (55) are solved using the tridiagonal algorithm, Reference 10. Equation (53) is rewritten in the form

$$P_{5j}\phi_{j-1} + P_{2j}\phi_j + P_{4j}\phi_{j+1} = R_{P_j} , \quad (56)$$

where the subscript has been added to the P coefficients to indicate the j node at which they are evaluated; the i and k subscripts have been dropped from the unknown ϕ values for simplicity; and R_{P_j} denotes the right side of Equation (53). A recursion relation is assumed,

$$\phi_j = q_j - b_j\phi_{j+1} , \quad (57)$$

and substitution of Equation (57) into Equation (56) yields

$$\phi_j = \frac{R_{P_j} - P_{5j}q_{j-1}}{P_{2j} - P_{5j}b_{j-1}} - \frac{P_{4j}\phi_{j+1}}{P_{2j} - P_{5j}b_{j-1}} . \quad (58)$$

From a comparison of Equations (57) and (58), it follows that

$$q_j = \frac{R_{P_j} - P_{5j}q_{j-1}}{P_{2j} - P_{5j}b_{j-1}} \quad (59)$$

and

$$b_j = \frac{P_{4j}}{P_{2j} - P_{5j}b_{j-1}} . \quad (60)$$

To initialize the solution, Equation (56) is written for j = 2,

$$\phi_2 = \frac{R_{P_2}}{P_{22}} - \frac{P_{42}}{P_{22}} \phi_3 \cdot \tag{61}$$

According to the recursion formula,

$$\phi_2 = q_2 - b_2 \phi_3 \, , \tag{62}$$

and it follows from a comparison of Equations (61) and (62) that

$$q_2 = \frac{R_{P_2}}{P_{22}} \tag{63}$$

and

$$b_2 = \frac{P_{42}}{P_{22}} \cdot \tag{64}$$

It follows directly from the recursion formula that

$$\phi_J = q_J \cdot \tag{65}$$

The three Poisson equations for the velocity components are solved by sweeping through the computational domain applying the recursion formula given by Equation (58). The manner in which the solution of the Poisson-type equations is coupled to the solution of the transport-type equations is discussed in Section 3.4.

3.2 Discretization of the Transport-Type Equations

As given in Section 2, the transport equations for the vorticity components, the turbulent kinetic energy, and the dissipation of turbulent kinetic energy can be written in the form

$$\alpha_\phi \alpha_1^2 \frac{\partial^2 \phi}{\partial \bar{x}^2} + \alpha_\phi \beta_1^2 \frac{\partial^2 \phi}{\partial \bar{y}^2} + \alpha_\phi \gamma_1^2 \frac{\partial^2 \phi}{\partial \bar{z}^2} + (\alpha_\phi \alpha_2 + \beta_\phi \alpha_1) \frac{\partial \phi}{\partial \bar{x}}$$

$$+ (\alpha_\phi \beta_2 + \gamma_\phi \beta_1) \frac{\partial \phi}{\partial \bar{y}} + (\alpha_\phi \gamma_2 + \delta_\phi \gamma_1) \frac{\partial \phi}{\partial \bar{z}} = \bar{\sigma}_\phi \ , \tag{66}$$

where $\phi = \Omega_x$, Ω_y, Ω_z, k, or ε.

Equation (66) cannot be solved for an arbitrary Reynolds number using the conventional central-difference approximations to the derivatives. The reason for this difficulty is that the coefficients of the convective terms $\partial\phi/\partial\bar{x}$, $\partial\phi/\partial\bar{y}$, and $\partial\phi/\partial\bar{z}$ contain the Reynolds number as a multiplicative factor. Consequently, with the standard central-difference algorithm, the discretized system of equations is diagonally dominant for only a limited range in Reynolds number. Diagonal dominance is necessary to obtain convergence in the iterative solution of the discretized system of equations.

In the present work the transport-type equations are discretized using Agarwal's third-order-accurate upwind-difference scheme, References 11 and 12. In the application of this method, Equation (66) is rewritten in the form

$$\Lambda_1 \frac{\partial^2 \phi}{\partial \bar{x}^2} + \Lambda_2 \frac{\partial^2 \phi}{\partial \bar{y}^2} + \Lambda_3 \frac{\partial^2 \phi}{\partial \bar{z}^2} - \Gamma_1 \frac{\partial \phi}{\partial \bar{x}} - \Gamma_2 \frac{\partial \phi}{\partial \bar{y}} - \Gamma_3 \frac{\partial \phi}{\partial \bar{z}} = \bar{\sigma}_\phi \ , \tag{67}$$

where

$$\Lambda_1 = \alpha_\phi \alpha_1^2 \tag{68}$$

$$\Lambda_2 = \alpha_\phi \beta_1^2 \tag{69}$$

$$\Lambda_3 = \alpha_\phi \gamma_1^2 \tag{70}$$

$$\Gamma_1 = -(\alpha_\phi \alpha_2 + \beta_\phi \alpha_1) \tag{71}$$

$$\Gamma_2 = -(\alpha_\phi \beta_2 + \gamma_\phi \beta_1) \tag{72}$$

$$\Gamma_3 = -(\alpha_\phi \gamma_2 + \delta_\phi \gamma_1) \ . \tag{73}$$

The basis of the upwind-difference algorithm can be illustrated by considering the term $\partial\phi/\partial\bar{x}$ in Equation (67). At an interior point (i,j,k) in the nodal network, this term is evaluated in terms of the adjacent points in the $\bar{x}$ direction with the following truncated Taylor-series representation and standard central-difference approximation to the first derivative:

$$\left.\frac{\partial\phi}{\partial\bar{x}}\right|_{i,j,k} = \frac{\phi_{i+1,j,k} - \phi_{i-1,j,k}}{2h} - \frac{h^2}{6}\left.\frac{\partial^3\phi}{\partial\bar{x}^3}\right|_{i,j,k} - \frac{h^4}{5!}\left.\frac{\partial^5\phi}{\partial\bar{x}^5}\right|_{i,j,k} . \tag{74}$$

In the third-order-accurate upwind-difference scheme, the derivative $\partial^3\phi/\partial\bar{x}^3$ is retained and expressed in terms of one-sided difference approximations depending on the sign of Γ:

$$\left.\frac{\partial^3\phi}{\partial\bar{x}^3}\right|_i = \frac{\left.\frac{\partial^2\phi}{\partial\bar{x}^2}\right|_i - \left.\frac{\partial^2\phi}{\partial\bar{x}^2}\right|_{i-1}}{h} \quad \text{if } \Gamma_1 > 0. \tag{75}$$

$$\left.\frac{\partial^3\phi}{\partial\bar{x}^3}\right|_i = \frac{\left.\frac{\partial^2\phi}{\partial\bar{x}^2}\right|_{i+1} - \left.\frac{\partial^2\phi}{\partial\bar{x}^2}\right|_i}{h} \quad \text{if } \Gamma_1 < 0. \tag{76}$$

Using Equations (75) and (76), it follows that

$$-\Gamma_1\left.\frac{\partial\phi}{\partial\bar{x}}\right|_i = -\Gamma_1\left(\frac{2\phi_{i+1} + 3\phi_i - 6\phi_{i-1} + \phi_{i-2}}{6h}\right), \text{ if } \Gamma_1 > 0 , \tag{77}$$

and

$$-\Gamma_1\left.\frac{\partial\phi}{\partial\bar{x}}\right|_i = -\Gamma_1\left(\frac{-\phi_{i+2} + 6\phi_{i+1} - 3\phi_i - 2\phi_{i-1}}{6h}\right), \text{ if } \Gamma_1 < 0 , \tag{78}$$

Analogous formulas apply to the terms $-\Gamma_2 (\partial\phi/\partial\bar{y})$ and $-\Gamma_3 (\partial\phi/\partial\bar{z})$ appearing in Equation (67). The terms $\partial^2\phi/\partial\bar{x}^2$, $\partial^2\phi/\partial\bar{y}^2$, and $\partial^2\phi/\partial\bar{z}^2$ and the derivatives appearing in the coefficients and source term are discretized using the standard central-difference approximations, Equations (38) through (43).

With this approach, the following is the finite-difference form of the transport-type equation:

$$T_1\phi_{i+2,j,k} + T_2\phi_{i+1,j,k} + T_3\phi_{i,j,k} + T_4\phi_{i-1,j,k} + T_5\phi_{i-2,j,k}$$
$$+ T_6\phi_{i,j+2,k} + T_7\phi_{i,j+1,k} + T_8\phi_{i,j-1,k} + T_9\phi_{i,j-2,k}$$
$$+ T_{10}\phi_{i,j,k+2} + T_{11}\phi_{i,j,k+1} + T_{12}\phi_{i,j,k-1} + T_{13}\phi_{i,j,k-2}$$
$$= T_{14} . \qquad (79)$$

The coefficients T_1 through T_{13} for the two cases $\Gamma_1 > 0$, $\Gamma_2 > 0$, $\Gamma_3 > 0$ and $\Gamma_1 < 0$, $\Gamma_2 < 0$, $\Gamma_3 < 0$ are defined in Table 1 along with the generalized form of the coefficients used in the calculations. When Equation (79) is applied at the second node from a boundary plane, the value of ϕ at the boundary is determined from the boundary condition and is transferred to the right side of the equation. When Equation (79) is applied at the interior node adjacent to the boundary plane, the value of ϕ at the boundary is determined again from the boundary condition, and the value of ϕ at the external node adjacent to the boundary is determined either from an image condition or extrapolation using the techniques discussed in Section 3.3; the known values are transferred to the right side of the equation. To solve for ϕ along a line of variable j, Equation (79) is written in the matrix form as follows:

TABLE 1. COEFFICIENTS IN THE DISCRETIZED FORM OF THE TRANSPORT EQUATION.

	$\Gamma_1>0, \Gamma_2>0, \Gamma_3>0$	$\Gamma_1<0, \Gamma_2<0, \Gamma_3<0$	Generalized Form
T_1	0	$-\frac{h}{6}\lvert\Gamma_1\rvert$	$\frac{h}{12}(\Gamma_1 - \lvert\Gamma_1\rvert)$
T_2	$\Lambda_1 - \frac{h}{3}\lvert\Gamma_1\rvert$	$\Lambda_1 + h\lvert\Gamma_1\rvert$	$\Lambda_1 + \frac{h}{3}(\lvert\Gamma_1\rvert - 2\Gamma_1)$
T_3	$-(2\Lambda_1 + 2\Lambda_2 + 2\Lambda_3 + \frac{h}{2}\lvert\Gamma_1\rvert + \frac{h}{2}\lvert\Gamma_2\rvert + \frac{h}{2}\lvert\Gamma_3\rvert)$	$-(2\Lambda_1 + 2\Lambda_2 + 2\Lambda_3 + \frac{h}{2}\lvert\Gamma_1\rvert + \frac{h}{2}\lvert\Gamma_2\rvert + \frac{h}{2}\lvert\Gamma_3\rvert)$	$-(2\Lambda_1 + 2\Lambda_2 + 2\Lambda_3 + \frac{h}{2}\lvert\Gamma_1\rvert + \frac{h}{2}\lvert\Gamma_2\rvert + \frac{h}{2}\lvert\Gamma_3\rvert)$
T_4	$\Lambda_1 + h\lvert\Gamma_1\rvert$	$\Lambda_1 - \frac{h}{3}\lvert\Gamma_1\rvert$	$\Lambda_1 + \frac{h}{3}(\lvert\Gamma_1\rvert + 2\Gamma_1)$
T_5	$-\frac{h}{6}\lvert\Gamma_1\rvert$	0	$-\frac{h}{12}(\Gamma_1 + \lvert\Gamma_1\rvert)$
T_6	0	$-\frac{h}{6}\lvert\Gamma_2\rvert$	$\frac{h}{12}(\Gamma_2 - \lvert\Gamma_2\rvert)$
T_7	$\Lambda_2 - \frac{h}{3}\lvert\Gamma_2\rvert$	$\Lambda_2 + h\lvert\Gamma_2\rvert$	$\Lambda_2 + \frac{h}{3}(\lvert\Gamma_2\rvert - 2\Gamma_2)$
T_8	$\Lambda_2 + h\lvert\Gamma_2\rvert$	$\Lambda_2 - \frac{h}{3}\lvert\Gamma_2\rvert$	$\Lambda_2 + \frac{h}{3}(\lvert\Gamma_2\rvert + 2\Gamma_2)$
T_9	$-\frac{h}{6}\lvert\Gamma_2\rvert$	0	$-\frac{h}{12}(\Gamma_2 + \lvert\Gamma_2\rvert)$
T_{10}	0	$-\frac{h}{6}\lvert\Gamma_3\rvert$	$\frac{h}{12}(\Gamma_3 - \lvert\Gamma_3\rvert)$
T_{11}	$\Lambda_3 - \frac{h}{3}\lvert\Gamma_3\rvert$	$\Lambda_3 + h\lvert\Gamma_3\rvert$	$\Lambda_3 + \frac{h}{3}(\lvert\Gamma_3\rvert - 2\Gamma_3)$
T_{12}	$\Lambda_3 + h\lvert\Gamma_3\rvert$	$\Lambda_3 - \frac{h}{3}\lvert\Gamma_3\rvert$	$\Lambda_3 + \frac{h}{3}(\lvert\Gamma_3\rvert + 2\Gamma_3)$
T_{13}	$-\frac{h}{6}\lvert\Gamma_3\rvert$	0	$-\frac{h}{12}(\Gamma_3 + \lvert\Gamma_3\rvert)$

GP21-0078-18

$$
\begin{bmatrix}
T_3 & T_7 & T_6 & & & & & & & & & & & & \\
T_8 & T_3 & T_7 & T_6 & & & & & & & & & & & \\
T_9 & T_8 & T_3 & T_7 & T_6 & & & & & & & & & & \\
 & T_9 & T_8 & T_3 & T_7 & T_6 & & & & & & & & & \\
 & & \ddots & \ddots & \ddots & \ddots & \ddots & & & & & & & & \\
 & & & \ddots & \ddots & \ddots & \ddots & \ddots & & & & & & & \\
 & & & & T_9 & T_8 & T_3 & T_7 & T_6 & & & & & & \\
 & & & & & \ddots & \ddots & \ddots & \ddots & \ddots & & & & & \\
 & & & & & & \ddots & \ddots & \ddots & \ddots & \ddots & & & & \\
 & & & & & & & \ddots & \ddots & \ddots & \ddots & \ddots & & & \\
 & & & & & & & & \ddots & \ddots & \ddots & \ddots & \ddots & & \\
 & & & & & & & & & \ddots & \ddots & \ddots & \ddots & \ddots & \\
 & & & & & & & & & T_9 & T_8 & T_3 & T_7 & T_6 & \\
 & & & & & & & & & & T_9 & T_8 & T_3 & T_7 & T_6 \\
 & & & & & & & & & & & T_9 & T_8 & T_3 & T_7 \\
 & & & & & & & & & & & & T_9 & T_8 & T_3
\end{bmatrix}
\begin{bmatrix}
\phi_{i,3,k} \\
\phi_{i,4,k} \\
\phi_{i,5,k} \\
\phi_{i,6,k} \\
\vdots \\
\phi_{i,j,k} \\
\vdots \\
\phi_{i,J-4,k} \\
\phi_{i,J-3,k} \\
\phi_{i,J-2,k} \\
\phi_{i,J-1,k}
\end{bmatrix}
=
\begin{bmatrix}
R_{T_{i,3,k}} \\
R_{T_{i,4,k}} \\
R_{T_{i,5,k}} \\
R_{T_{i,6,k}} \\
\vdots \\
R_{T_{i,j,k}} \\
\vdots \\
R_{T_{i,J-4,k}} \\
R_{T_{i,J-3,k}} \\
R_{T_{i,J-2,k}} \\
R_{T_{i,J-1,k}}
\end{bmatrix}
\tag{80}
$$

Equation (80) represents a system of simultaneous linear equations with a coefficient matrix of band structure having a total band width of five. The system is solved using SUBROUTINE GELB from the McDonnell Douglas Automation Company Scientific Subroutine Package, Reference 13, a routine which performs Gaussian elimination with column pivoting to solve the matrix problem.

The solution sequence of the transport-type equations is discussed in Section 3.4.

3.3 Discretization of the Boundary Conditions

As discussed in Section 2.3, boundary conditions imposed in the flowfield analysis are of either the Dirichlet or Neumann type. The discretized forms of these boundary conditions are discussed in this section.

On an inflow plane where the velocity and turbulence property profiles are specified analytically, the boundary conditions given by Equation (28) are expressed as known functions of the discretized coordinates,

$$u_{i,J,k} = u(x_i, \tilde{h}, z_k),\ v_{i,J,k} = v(x_i, \tilde{h}, z_k),\ w_{i,J,k} = w(x_i, \tilde{h}, z_k),$$

$$k_{i,J,k} = k(x_i, \tilde{h}, z_k), \text{ and } \varepsilon_{i,J,k} = \varepsilon(x_i, \tilde{h}, z_k). \tag{81}$$

The vorticity profiles are computed by differentiating the analytic velocity profiles according to Equations (29) through (31), and the resulting expressions are given as functions of the discretized coordinates,

$$\Omega_{x_{i,J,k}} = \Omega_x(x_i, \tilde{h}, z_k),\ \Omega_{y_{i,J,k}} = \Omega_y(x_i, \tilde{h}, z_k),$$

$$\text{and } \Omega_{z_{i,J,k}} = \Omega_z(x_i, \tilde{h}, z_k). \tag{82}$$

On solid surfaces the velocity components and turbulent kinetic energy are expressed in finite-difference form; for example, on the ground plane

$$u_{i,2,k} = v_{i,2,k} = w_{i,2,k} = k_{i,2,k} = 0. \tag{83}$$

On the ground plane the turbulent dissipation follows directly from Equation (33) using a one-sided difference formula to represent the second derivative of the turbulent kinetic energy,

$$\varepsilon_{i,2,k} = \beta_{1,2}^2 \left(\frac{4k_{i,4,k} - k_{i,5,k} - 5k_{i,3,k}}{h^2} \right) . \tag{84}$$

The vorticity components on a solid surface are discretized using the approach developed by Woods, Reference 14. Consider Ω_x evaluated on the surface $y = 0$. Since $v = 0$ on the ground plane, Equation (29) reduces to

$$\Omega_x = \frac{\partial w}{\partial y} = \beta_1 \frac{\partial w}{\partial \bar{y}} . \tag{85}$$

It follows that $\partial\Omega_x/\partial y = \partial^2 w/\partial y^2$, or in terms of the transformed y coordinate,

$$\beta_1 \frac{\partial \Omega_x}{\partial \bar{y}} = \beta_1^2 \frac{\partial^2 w}{\partial \bar{y}^2} + \beta_2 \frac{\partial w}{\partial \bar{y}} . \tag{86}$$

Using a Taylor series, w at the node adjacent to the wall is represented by the following expansion:

$$w_{i,3,k} = w_{i,2,k} + \left.\frac{\partial w}{\partial \bar{y}}\right|_{i,2,k} h + \frac{1}{2} \left.\frac{\partial^2 w}{\partial \bar{y}^2}\right|_{i,2,k} h^2 . \tag{87}$$

When Equations (83), (84), and (85) are introduced, Equation (87) becomes

$$w_{i,3,k} = \frac{\Omega_{x_{i,2,k}}\, h}{\beta_{1,2}} + \frac{h^2}{2\,\beta_{1,2}} \left.\frac{\partial \Omega_x}{\partial \bar{y}}\right|_{i,2,k} - \frac{\beta_{2,2}\, h^2\, \Omega_{x_{i,2,k}}}{\beta_{1,2}^3} . \tag{88}$$

A one-sided difference formula is used to represent the vorticity derivative,

$$\frac{\partial \Omega_x}{\partial \bar{y}} = \frac{\Omega_{x_{i,3,k}} - \Omega_{x_{i,2,k}}}{h} , \tag{89}$$

and Equation (88) is solved for the wall vorticity:

$$\Omega_{x_{i,2,k}} = \frac{2\,\beta_{1,2}^3\, w_{i,3,k} - \beta_{1,2}^2\, \Omega_{x_{i,3,k}}\, h}{\beta_{1,2}^2\, h - \beta_{2,2}\, h^2} . \tag{90}$$

On the ground plane

$$\Omega_{y_{i,2,k}} = 0 \tag{91}$$

and

$$\Omega_{z_{i,2,k}} = \frac{2\,\beta_{1,2}^{3}\,u_{i,3,k} + \beta_{1,2}^{2}\,\Omega_{z_{i,3,k}}\,h}{\beta_{2,2}\,h^{2} - \beta_{1,2}^{2}\,h} \,. \tag{92}$$

On outflow and symmetry planes where the normal gradients vanish, the derivatives expressed by Equations (34) through (36) are represented in discrete form using a one-sided finite-difference formula. For example, consider the condition $\partial\phi/\partial\bar{x} = 0$ evaluated on the plane $x = 0$ ($i = 2$):

$$\left.\frac{\partial\phi}{\partial\bar{x}}\right|_{2,j,k} = \frac{4\phi_{3,j,k} - \phi_{4,j,k} - 3\phi_{2,j,k}}{2h} = 0, \tag{93}$$

which results in the boundary value of ϕ being given by

$$\phi_{2,j,k} = \frac{4}{3}\,\phi_{3,j,k} - \frac{1}{3}\,\phi_{4,j,k} \,. \tag{94}$$

In the solution of the transport-type equations, values of the flow properties are required on planes external to the boundaries of the computational domain and spaced a distance h from the latter. If the gradient of the flow property vanishes on the computational boundary, the external plane is an image plane and the value of the property is determined by the vanishing gradient. For example, at the surface $x = 0$ ($i = 2$),

$$\left.\frac{\partial\phi}{\partial\bar{x}}\right|_{2,j,k} = \frac{\phi_{1,j,k} - \phi_{3,j,k}}{2h} = 0 \,, \tag{95}$$

and

$$\phi_{1,j,k} = \phi_{3,j,k} \,. \tag{96}$$

If the gradient does not vanish, the flow property on the external plane is evaluated from a quadratic extrapolation formula. For example,

$$\phi_{1,j,k} = 3\phi_{2,j,k} - 3\phi_{3,j,k} + \phi_{4,j,k} \,. \tag{97}$$

In discretization of the boundary conditions, special attention had to be given to evaluating velocity components normal to the outflow boundaries. Through the use of the coordinate transformations, the boundary conditions on the outflow surfaces are specified in the far field. The level of the normal velocity component is not specified; rather, its normal derivative is set to zero, and the level of the velocity is computed as part of the solution. It was found that following the achievement of a convergent flowfield, an integral mass balance performed on the computational domain failed to satisfy continuity within an acceptable tolerance. Consequently, a technique was devised to modify the normal velocity component on each outflow plane in the manner described below.

The mass flow rate across each boundary of the solution domain is computed using trapezoidal integration. For example, on the plane $\bar{x} = \bar{L}$, the normalized mass flow rate is given by

$$\dot{m}_{\bar{x}=\bar{L}} = \int_0^{\bar{H}} \int_0^{\bar{W}} \frac{|u| \cos\theta}{\beta_1 \gamma_1} \, d\bar{z} d\bar{y}$$

$$(u > 0, \cos\theta = 1; \; u < 0, \cos\theta = -1). \tag{98}$$

A ratio is then formed of the net flow into the computational domain to the net flow from the computational domain, and the normal velocity component computed from the formula given by Equation (94) is multiplied by the ratio every 10 iterations in the solution cycle. As the flow-variable residuals decline, the mass flow rate approaches unity and the net mass flow rate reduces to 10^{-15}.

Specific boundary conditions for the flow configurations considered are defined in Section 4.

3.4 Solution of the Coupled System of Equations

The sequence in which the solution of the Poisson- and transport-type equations is carried out is illustrated in Figure 4. Initial distributions are established for all flow properties. The Poisson equations are solved for the velocity components using the tridiagonal algorithm and alternating-direction line iteration in which the values of the velocity components are updated according to the formula

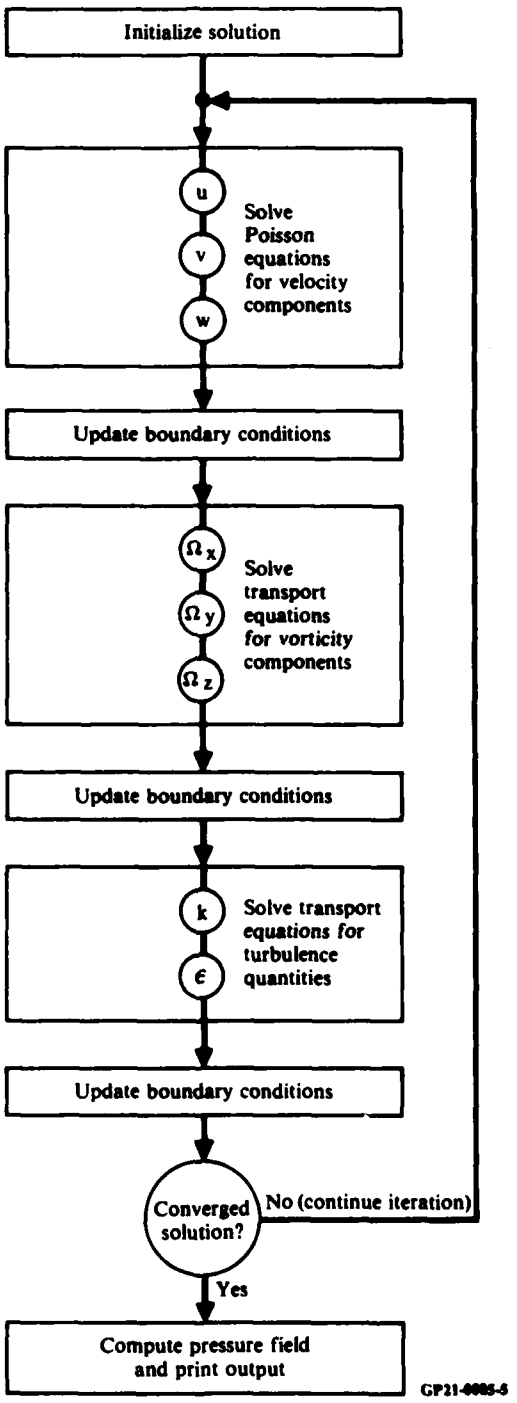

Figure 4. Computing sequence used in the solution of the flowfield equations.

$$\phi^{n+1}_{i,j,k} = \phi^{n-1}_{i,j,k} + R\left(\phi^{n}_{i,j,k} - \phi^{n-1}_{i,j,k}\right), \tag{99}$$

where n is the iteration counter and R is the relaxation factor, which has a value of 1.2 for the Poisson equations. The transport-type equations are solved for the vorticity components and turbulence quantities using the penta-diagonal algorithm (GELB) and alternating-direction line iteration in which the properties are updated according to Equation (99) with R ranging from 0.2 to 0.8 depending upon the jet configuration. As soon as a flow variable has been recomputed, the associated boundary conditions are re-evaluated. Convergence is considered to have been achieved when the root-mean-square residual for each variable,

$$r_{\phi} = \sqrt{\sum_{ijk}\left(\phi^{n+1}_{i,j,k} - \phi^{n}_{i,j,k}\right)^2}\Big/ h , \tag{100}$$

has reached a specified level (10^{-4} to 10^{-6} depending upon the magnitude of the unknown).

The flowfield calculations in the present work were done using the CDC 7600 computer of the Systems Technology Program - System Simulation Center operated by the McDonnell Douglas Astronautics Company, Huntington Beach, for the Department of the Army.

Flowfields were computed for isolated and interacting jets. The maximum Reynolds number for which convergent solutions could be achieved was on the order of 10^2 using the finest finite-difference grid permitted by the available storage capacity of the CDC 7600. Each of these solutions required approximately 1 h of machine computation time. Definitions of the flow configurations and comparisons of the calculated properties with data are presented in the next section.

4. THE COMPUTED FLOWFIELDS

Under the present contract, turbulent flowfields were calculated for isolated and interacting jets in ground effect. For the single jet, both normal and inclined impingement were considered, and for the two jets, both equal and unequal nozzle diameters were considered. In this section, calculated flow variables are presented for these configurations (as well as for a laminar-flow test problem), and comparisons are made between computed and measured properties.

4.1 Laminar Channel Flow

In order to establish the accuracy of the numerical algorithm for solution of the Navier-Stokes equations, laminar flow in a channel was computed as one of the standard problems considered in evaluation of any new finite-difference method. A quarter-section of the channel is shown in Figure 5(a), where the half-width is denoted by W, the half-height by H, and the length by L. Since the entering flow is taken to be symmetric with respect to the channel midplanes $y = 0$ and $z = 0$, only a quarter section of the passage need be computed. In this problem, the aspect ratio of the channel is unity ($W = H$) and L is equal to 20W. Normalizing by the channel width 2W, the dimensions of the physical solution domain in the x, y, and z directions are 10.0, 0.5, and 0.5, respectively.

For this problem, a coordinate transformation is used in the x direction only, where the computational coordinate $\bar{x}$ (normalized by the channel width) is related to the physical x by the following expression:

$$\bar{x} = \frac{2.2x}{1 + x} \, . \tag{100}$$

(a) Computational domain

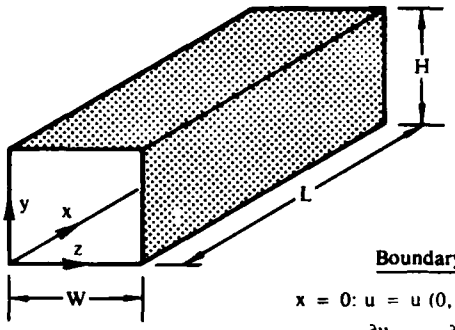

Boundary conditions

$x = 0$: $u = u(0, y, z)$, $v = 0$, $w = 0$

$x = L$: $\frac{\partial u}{\partial x} = 0$, $\frac{\partial v}{\partial x} = 0$, $\frac{\partial w}{\partial x} = 0$

$y = 0$: $\frac{\partial u}{\partial y} = 0$, $v = 0$, $\frac{\partial w}{\partial y} = 0$

$y = H$: $u = 0$, $v = 0$, $w = 0$

$z = 0$: $\frac{\partial u}{\partial z} = 0$, $\frac{\partial v}{\partial z} = 0$, $w = 0$

$z = W$: $u = 0$, $v = 0$, $w = 0$

(b) Centerline velocity variation

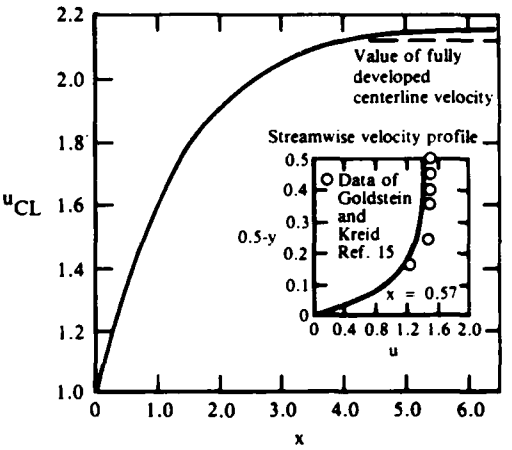

(c) Streamwise velocity profiles for z = 0

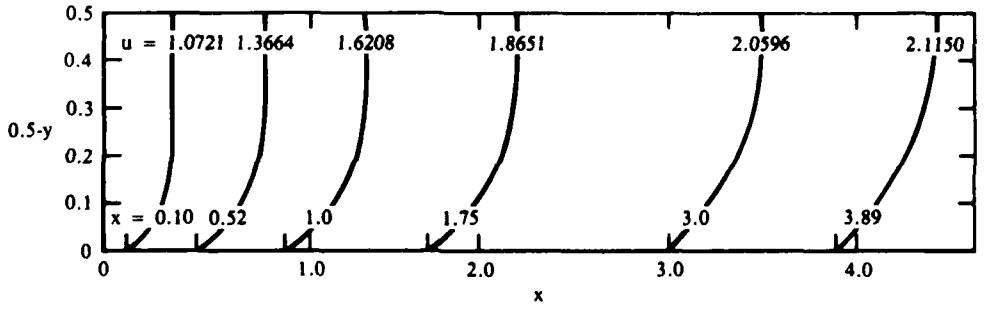

(d) Contour plots of the x-component of velocity for selected axial locations.

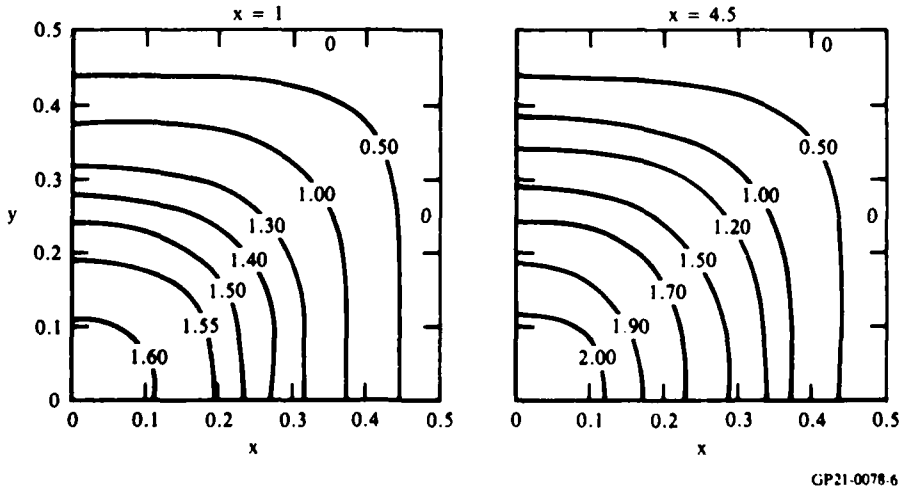

GP21-0078-6

Figure 5. Velocity profiles for laminar channel flow (Re = 75).

Values of x for uniform increments of $\bar{x}$ are tabulated below.

$\bar{x}$	x	$\bar{x}$	x
0.	0.	1.1	1.0000
0.1	0.0476	1.2	1.2000
0.2	0.1000	1.3	1.4444
0.3	0.1579	1.4	1.7500
0.4	0.2222	1.5	2.1429
0.5	0.2941	1.6	2.6667
0.6	0.3750	1.7	3.4000
0.7	0.4667	1.8	4.5000
0.8	0.5714	1.9	6.3333
0.9	0.6923	2.0	10.0000
1.0	0.8333		

Thus, the dimensions of the computational domain in the $\bar{x}$, $\bar{y}$, and $\bar{z}$ directions, respectively, are 2.0 x 0.5 x 0.5.

The boundary conditions for the velocity components are given in Figure 5(a). At the entrance plane to the channel, it is assumed that the flow is in the x direction only. Symmetry conditions are imposed on the planes y = 0 and z = 0, and the no-slip, impermeable-wall constraints are enforced at the solid surfaces x = W and y = H. At the outflow plane, the velocity components are taken to be invariant with x (fully developed flow).

The three-dimensional laminar channel flow was computed with Re = 75 (based on the channel width and entrance-plane velocity) using 42 grid points in the x direction, 12 in the y direction, and 12 in the z direction. The centerline velocity variation with the axial coordinate is shown in Figure 5(b), and the streamwise velocity profiles on the midplane z = 0 for selected x stations are shown in Figure 5(c). The slight difference between the numerical value of the fully developed centerline velocity and that determined analytically is attributed to the relative coarseness of the mesh, as is the small disparity between the numerical streamwise velocity profile for x = 0.57 and the data of Goldstein and Kreid, Reference 15. Two contour plots of the x-component of velocity are shown in Figure 5(d) which demonstrate the acceleration of the central core as the boundary layers develop on the confining walls.

4.2 Turbulent Isolated Jet-Impingement Flow

The first turbulent jet-impingement flow considered is that for an isolated nozzle with a free upper boundary and its axis perpendicular to the

ground, as illustrated in Figure 1(a) in planar view. The flowfield is established with specification of the nozzle height above ground, the velocity and turbulence profiles at the nozzle exit plane, and the Reynolds number based on the nozzle exit conditions.

In order to take advantage of symmetry, only a quarter of the jet flowfield is computed, as illustrated in Figure 6(a). The top of the computational domain is not at the nozzle exit plane but rather is located a distance $\tilde{h}$ above the ground. The solution domain extends a distance L in the x direction and a distance W in the z direction. In this problem the width and depth are taken to be equal (L = W), and the dimensions of the physical domain normalized by the jet nozzle diameter are chosen to be L = 2.0, $\tilde{h}$ = 1.5, and W = 2.0.

Coordinate transformations are used in both the x and z directions, where the computational coordinates $\bar{x}$ and $\bar{z}$ (normalized by the nozzle diameter) are expressed in terms of the physical coordinates through the following relations:

$$\bar{x} = \frac{2.25x}{1 + x} \tag{102}$$

$$\bar{z} = \frac{2.25z}{1 + z} \, . \tag{103}$$

Values of x and z for uniform increments of $\bar{x}$ and $\bar{z}$ are listed below.

$\bar{x}$, $\bar{z}$	x, z
0.	0.
0.1	0.0465
0.2	0.0976
0.3	0.1538
0.4	0.2162
0.5	0.2857
0.6	0.3636
0.7	0.4516
0.8	0.5517
0.9	0.6667
1.0	0.8000
1.1	0.9565
1.2	1.1429
1.3	1.3684
1.4	1.6471
1.5	2.0000

The dimensions of the computational domain are 1.5 x 1.5 x 1.5 in the $\bar{x}$, $\bar{y}$ and $\bar{z}$ directions, respectively.

The velocity profile at the inflow plane is assumed to be fully developed and given by the relation

$$v(x, \tilde{h}, z) = - \frac{1}{1 + Kr^2} , \tag{104}$$

where K is a constant for a fixed value of $\tilde{h}$ and r is the distance along the perpendicular from points within the inflow plane to the jet centerline:

$$K = \frac{0.414}{(\delta/D)^2} \tag{105}$$

$$r^2 = x^2 + z^2. \tag{106}$$

In Equation (105) δ is the jet half-radius at a distance $(H - \tilde{h})$ below the nozzle exit plane and is computed from the empirical relations of Giralt, Chia, and Trass, Reference 16. Also on the inflow plane, $v = w = 0$, and k and ε follow from the assumed profiles given below.

$$k(x, \tilde{h}, z) = - 0.04v(x, \tilde{h}, z) \tag{107}$$

$$\varepsilon(x, \tilde{h}, z) = 5k(x, \tilde{h}, z)^{3/2} . \tag{108}$$

On the impingement surface the velocity components and the turbulent kinetic energy are zero, and the dissipation is determined from the reduced form of the turbulent-kinetic-energy transport equation at the wall. The boundary conditions follow from symmetry conditions for $x = 0$ and $z = 0$ and from the assumption of developed flow for $x = L$ and $z = W$.

The impinging-jet flowfield was computed for Re = 100 and H = 7.5 ($\tilde{h}$ = 1.5) using 17 grid points in each of the coordinate directions. Figure 6(b) illustrates the ground-plane pressure variation normalized by the stagnation-point pressure p_s, where p_∞ is the minimum pressure on the surface. The computed profile, which has been reflected about the symmetry plane $x = 0$, is compared with the experimental data of Snedeker and Donaldson, Reference 17, for the same value of H but for a Reynolds number on the order of 100 000.

(a) Computational domain

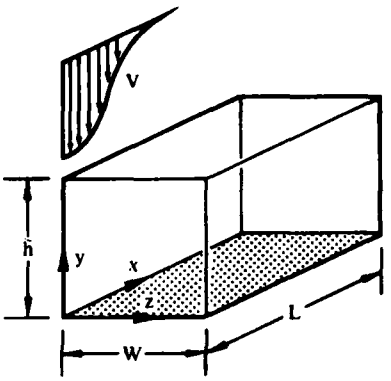

(b) Ground-plane pressure variaton for z = 0

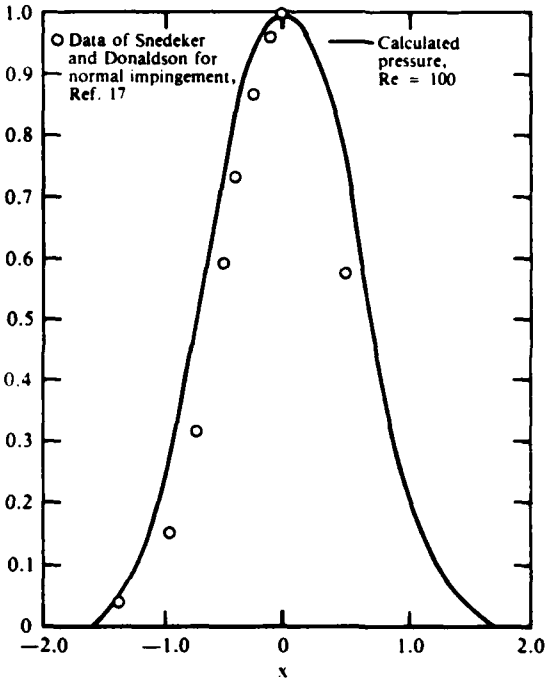

Boundary conditions

$x = 0$: $u = 0, \frac{\partial v}{\partial x} = 0, \frac{\partial w}{\partial x} = 0, \frac{\partial k}{\partial x} = 0, \frac{\partial \epsilon}{\partial x} = 0$

$x = L$: $\frac{\partial u}{\partial x} = 0, \frac{\partial v}{\partial x} = 0, \frac{\partial w}{\partial x} = 0, \frac{\partial k}{\partial x} = 0, \frac{\partial \epsilon}{\partial x} = 0$

$y = 0$: $u = 0, v = 0, w = 0, k = 0, \epsilon = \frac{1}{Re} \frac{\partial^2 k}{\partial y^2}$

$y = \tilde{h}$: $u = 0, v = v(x, \tilde{h}, z), w = 0, k = k(x, \tilde{h}, z), \epsilon = \epsilon(x, \tilde{h}, z)$

$z = 0$: $\frac{\partial u}{\partial z} = 0, \frac{\partial v}{\partial z} = 0, w = 0, \frac{\partial k}{\partial z} = 0, \frac{\partial \epsilon}{\partial z} = 0$

$z = W$: $\frac{\partial u}{\partial z} = 0, \frac{\partial v}{\partial z} = 0, \frac{\partial w}{\partial z} = 0, \frac{\partial k}{\partial z} = 0, \frac{\partial \epsilon}{\partial z} = 0$

(c) y-component of velocity for x = 0

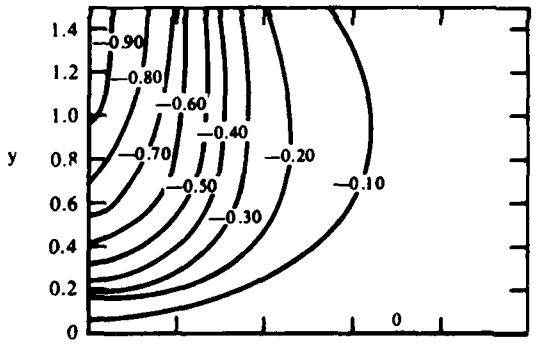

(d) z-component of velocity for x = 0

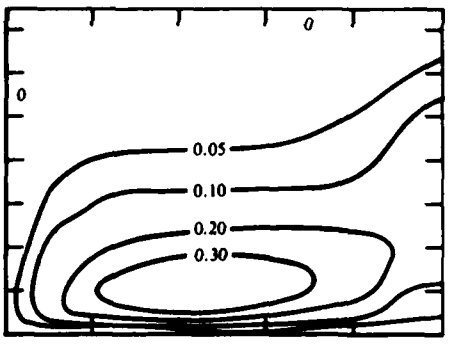

(e) x-component of vorticity for x = 0

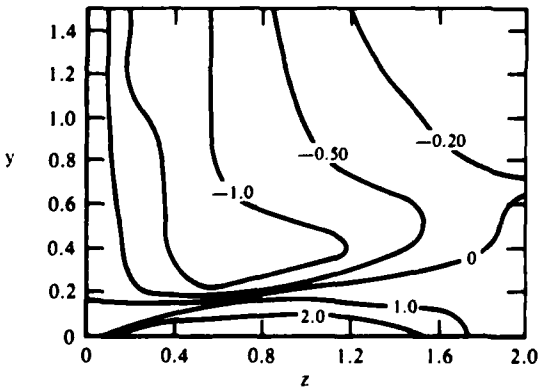

(f) Eddy viscosity for x = 0

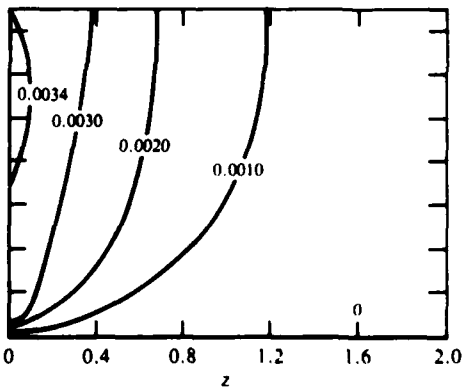

CP21-0078-7

Figure 6. Flow properties for an isolated jet with normal impingement.

For the same configuration, Figure 7(a), the ground-plane pressure and jet centerline velocity as a function of distance from the stagnation point normalized by the jet half-radius at the beginning of the impingement region are illustrated in Figures 7(b) and 7(c), respectively, and are compared with the experimental data of Giralt, Chia, and Trass, Reference 15. The length scale δ is clearly useful since it collapses the pressure and velocity profiles to a single curve for a range of H. The ground-plane pressure profile for $z = 0$ computed in the present work with $Re = 100$ compares reasonably well with the experimental results, which are not strongly dependent on Reynolds number since the surface pressure in the impingement region is governed by the dynamics of the flow. For this reason, the inviscid solution of Scholtz and Trass, Reference 18, which is also shown in Figure 7(b), agrees well with the data. The dimensionless centerline velocity decay of the impinging jet is plotted in Figure 7(c) as a function of the distance from the stagnation point normalized by the half-radius of the jet at the beginning of the impingement region. The present solution for $Re = 100$ follows the experimental centerline velocity variation obtained for Reynolds numbers of 30 000 to 80 000. However, the velocity decay computed by Scholtz and Trass, Reference 18, using inviscid theory overpredicts the magnitude of v. The reason for this discrepancy is that for $H/D > 7.78$, as is the case in the measurements, the impinging-jet velocity decay and spreading are appreciably affected by turbulent free-jet entrainment and viscous effects. For values of $H/D < 7.78$, the accuracy of the inviscid theory should improve, however, since the free-jet entrainment is small in such cases and the jet decay and spreading during the deflection are primarily governed by the presence of the wall.

A more complex isolated jet-impingement flow is formed when the nozzle centerline is inclined at an angle θ with respect to the ground plane. The computational domain for this configuration is illustrated in Figure 8(a). In this case there is only a single symmetry plane, and half the jet flowfield must be computed. The inflow plane is located at $y = \tilde{h}$; the outflow planes are at $x = 0$, $x = L$, and $z = W$; and the symmetry plane is at $z = 0$. For this problem $L = 4$, $\tilde{h} = 1.5$, and $W = 2$.

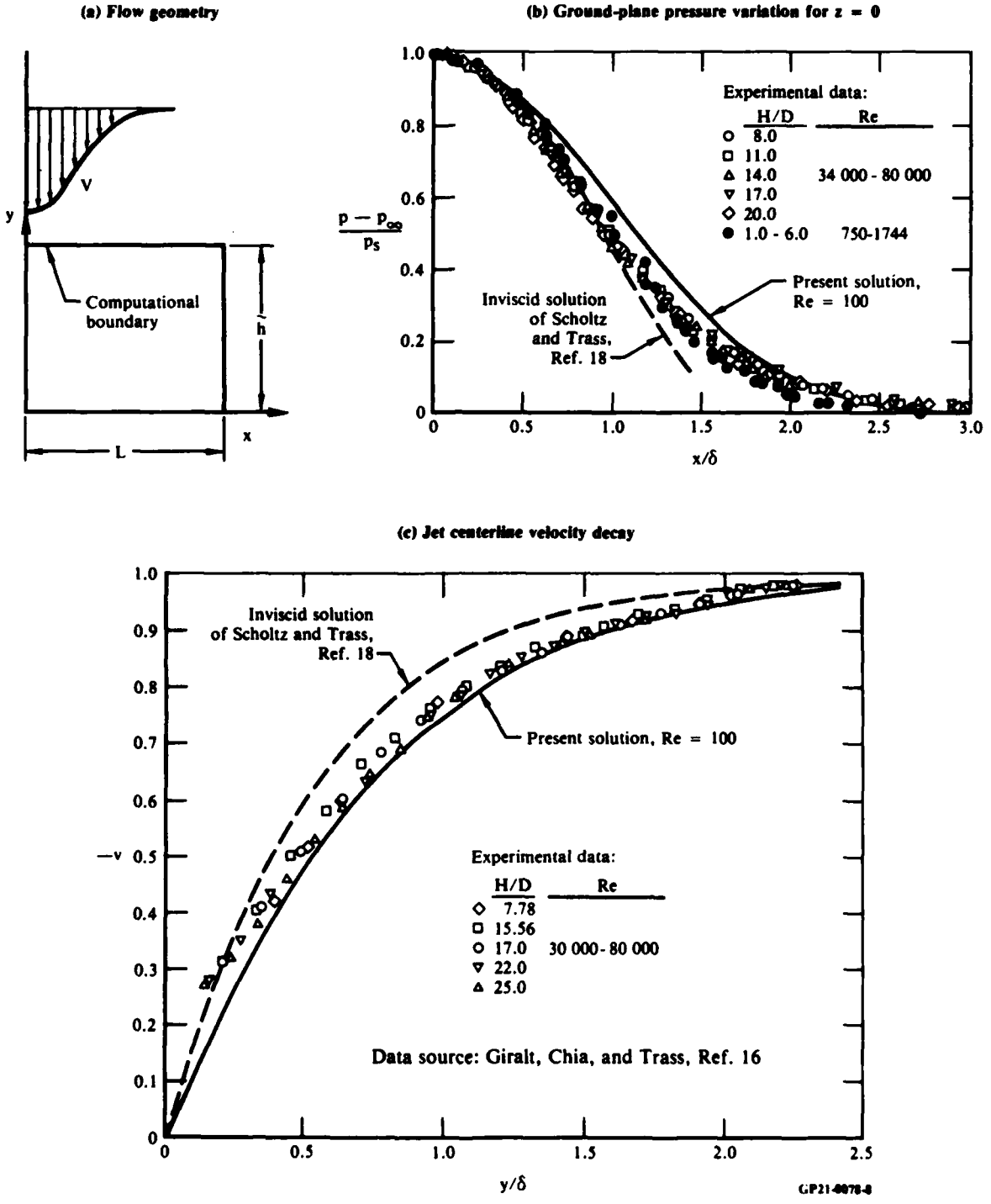

Figure 7. Flow properties for an isolated jet with normal impingement.

(a) Computational domain

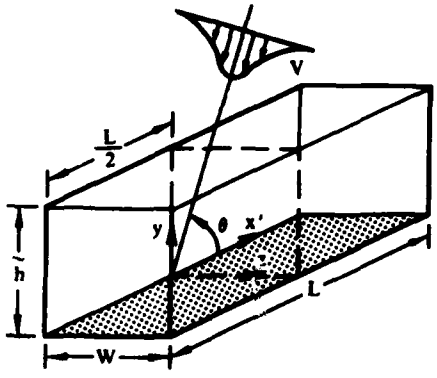

Boundary conditions

$x = -\frac{L}{2}: \frac{\partial u}{\partial x} = 0, \frac{\partial v}{\partial x} = 0, \frac{\partial w}{\partial x} = 0, \frac{\partial k}{\partial x} = 0, \frac{\partial \epsilon}{\partial x} = 0$

$x = \frac{L}{2}: \frac{\partial u}{\partial x} = 0, \frac{\partial v}{\partial x} = 0, \frac{\partial w}{\partial x} = 0, \frac{\partial k}{\partial x} = 0, \frac{\partial \epsilon}{\partial x} = 0$

$y = 0: u = 0, v = 0, w = 0, k = 0, \epsilon = \frac{1}{Re} \frac{\partial^2 k}{\partial y^2}$

$y = \tilde{h}: u = u(x, \tilde{h}, z), v = v(x, \tilde{h}, z), w = w(x, \tilde{h}, z),$

$k = k(x, \tilde{h}, z), \epsilon = \epsilon(x, \tilde{h}, z)$

$z = 0: \frac{\partial u}{\partial z} = 0, \frac{\partial v}{\partial z} = 0, w = 0, \frac{\partial k}{\partial z} = 0, \frac{\partial \epsilon}{\partial z} = 0$

$z = W: \frac{\partial u}{\partial z} = 0, \frac{\partial v}{\partial z} = 0, \frac{\partial w}{\partial z} = 0, \frac{\partial k}{\partial z} = 0, \frac{\partial \epsilon}{\partial z} = 0$

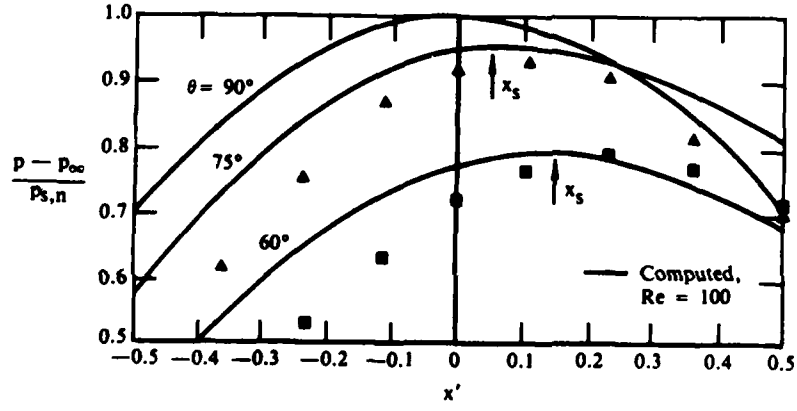

(b) Ground-plane pressure variation for z = 0 in the vicinity of the stagnation point x_s

▲ 75° } Data of Snedeker
■ 60° } and Donaldson, Ref. 17

(c) Stagnation-point pressure as a function of jet vector angle

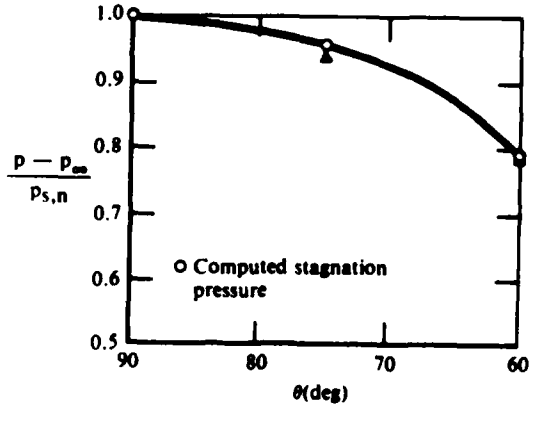

(d) Stagnation-point displacement as a function of jet vector angle

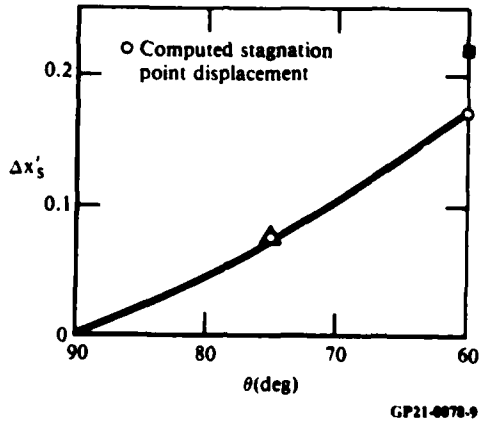

GP21-0078-9

Figure 8. Flow properties for an isolated jet with inclined impingement.

The following coordinate transformations are used in the x and z directions:

$$\bar{x} = \frac{0.75x}{3 - x} \qquad 0 \leq \bar{x} \leq 1.5 \tag{109}$$

$$\bar{x} = \frac{3.75x - 6}{x - 1} \qquad 1.5 < \bar{x} \leq 3.0 \tag{110}$$

$$\bar{z} = \frac{2.25z}{1 + z} \, . \tag{111}$$

Tabulated values of x and z for uniform increments in $\bar{x}$ and $\bar{z}$ are given below.

$\bar{x}$	x	$\bar{x}$	x
0.	0.	1.6	2.0465
0.1	0.3529	1.7	2.0976
0.2	0.6316	1.8	2.1538
0.3	0.8571	1.9	2.2162
0.4	1.0435	2.0	2.2857
0.5	1.2000	2.1	2.3636
0.6	1.3333	2.2	2.4516
0.7	1.4483	2.3	2.5517
0.8	1.5484	2.4	2.6667
0.9	1.6364	2.5	2.8000
1.0	1.7143	2.6	2.9565
1.1	1.7838	2.7	3.1429
1.2	1.8462	2.8	3.3684
1.3	1.9024	2.9	3.6471
1.4	1.9535	3.0	4.0000
1.5	2.0000		

$\bar{z}$	z
0.	0.
0.1	0.0465
0.2	0.0976
0.3	0.1538
0.4	0.2162
0.5	0.2857
0.6	0.3636
0.7	0.4516
0.8	0.5517
0.9	0.6667
1.0	0.8000
1.1	0.9565
1.2	1.1429
1.3	1.3684
1.4	1.6471
1.5	2.0000

The dimensions of the computational domain in the $\bar{x}$, $\bar{y}$, and $\bar{z}$ directions, respectively, are 3.0 x 1.5 x 1.5.

The velocity profile at the inflow plane is again assumed to be fully developed and is given by the relation

$$V(r) = - \frac{1}{1 + Kr^2} . \tag{112}$$

In Equation (112), K is the constant defined by Equation (105) and r is the distance along the perpendicular from points within the inflow plane to the jet centerline, which in this case is given by

$$r^2 = [(x - L/2) \sin \theta - y \cos \theta]^2 + z^2 . \tag{113}$$

The boundary values for the velocity components are given by the relations:

$$u(x, \tilde{h}, z) = V(r) \cos \theta \tag{114}$$

$$v(x, \tilde{h}, z) = V(r) \sin \theta \tag{115}$$

$$w(x, \tilde{h}, z) = 0. \tag{116}$$

The turbulent kinetic energy and dissipation are computed from Equations (107) and (108). The remaining boundary conditions on the impingement surface and the three outflow planes are defined in Figure 8(a).

The flowfield for this configuration was computed for Re = 100 and H = 7.5 ($\tilde{h}$ = 1.5) using 32 grid points in the $\bar{x}$ direction, 17 in the $\bar{y}$ direction, and 17 in the $\bar{z}$ direction. The computed impingement-plane pressure along the line z = 0 is shown in Figure 8(b) for $\theta = 90^o$, 75^o, and 60^o and compared with the data of Snedeker and Donaldson, Reference 17, for the case of inclined impingement. In this plot, p_∞ is the minimum surface pressure; $p_{s,n}$ is the stagnation-point pressure for normal impingement; and $x' = x - L/2$. The computed variations of the stagnation-point pressure and displacement as functions of the jet vector angle agree reasonably well with the data as shown in Figures 8(c) and 8(d). For the same inclined-jet configuration shown in Figure 9(a), Figures 9(b) through 9(e) illustrate the y component of velocity and the x component of velocity along the plane z = 0 for $\theta = 75^o$ and $\theta = 60^o$.

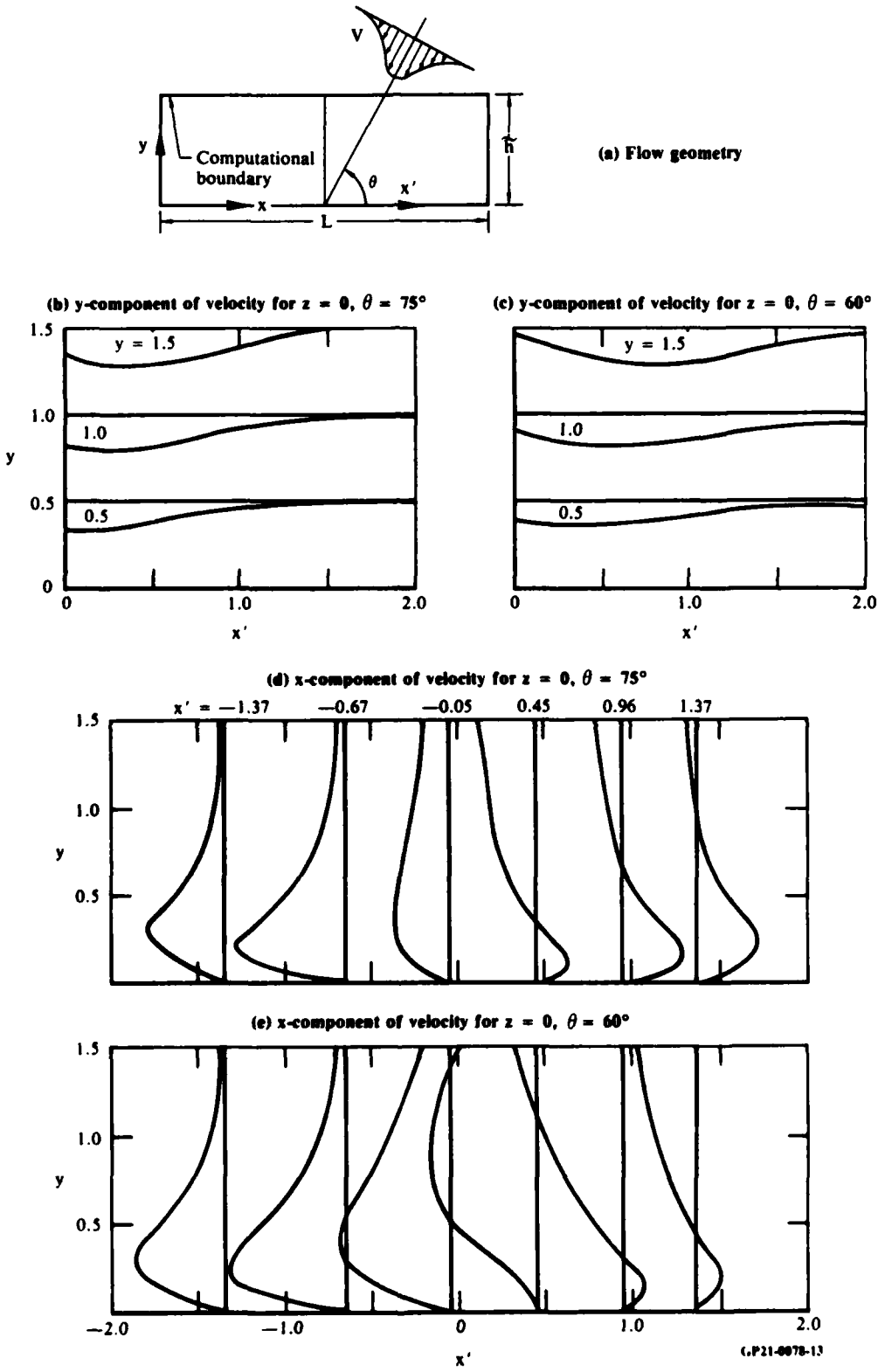

Figure 9. Flow properties for an isolated jet with inclined impingement.

A more complicated jet-impingement flow exists when the jet discharges through a blocking plate which is parallel and in proximity to the ground. In this case the flow separates on the upper surface, and a recirculating region must be treated in the analysis. The computational domain is illustrated in Figure 10(a), where a quarter of the jet is computed for normal impingement. The spacing between the plates is denoted by H, and the plate dimensions are WxL, where all lengths are normalized by the diameter of the entering jet. Taking L = W, the dimensions of the physical solution domain in the x, y, and z directions are 5.0 x 1.5 x 5.0, respectively.

For this problem, coordinate transformations are used in both the x and z directions, where the computational coordinates $\bar{x}$ and $\bar{z}$ are expressed in terms of the physical coordinates x and z by the following relations:

$$\bar{x} = \frac{1.8x}{1 + x} \tag{117}$$

$$\bar{z} = \frac{1.8z}{1 + z} . \tag{118}$$

Tabular values of x and z for uniform increments of the transformed coordinates are listed below.

$\bar{x}$, $\bar{z}$	x, z
0.	0.
0.1	0.0588
0.2	0.1250
0.3	0.2000
0.4	0.2857
0.5	0.3846
0.6	0.5000
0.7	0.6364
0.8	0.8000
0.9	1.0000
1.0	1.2500
1.1	1.5714
1.2	2.0000
1.3	2.6000
1.4	3.5000
1.5	5.0000

The dimensions of the computational domain are 1.5 x 1.5 x 1.5.

(a) Computational domain

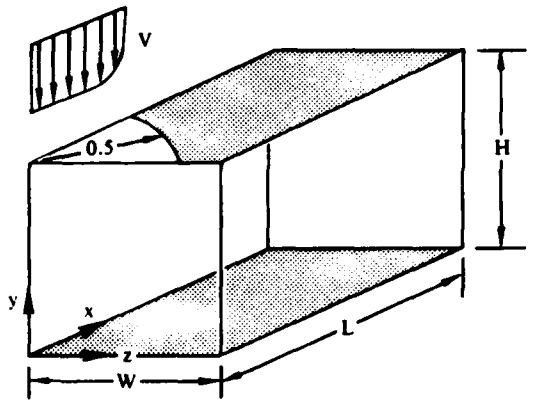

(b) Streamline pattern

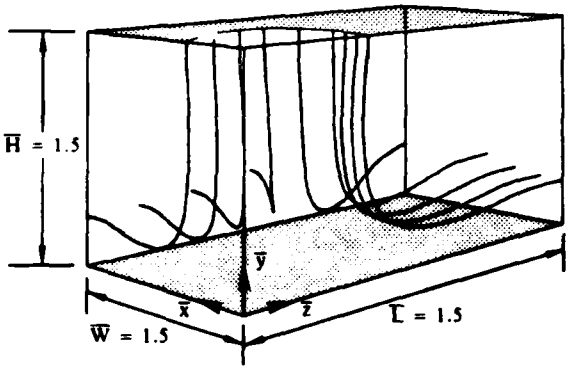

Boundary conditions

$x = 0$: $u = 0, \frac{\partial v}{\partial x} = 0, \frac{\partial w}{\partial x} = 0, \frac{\partial k}{\partial x} = 0, \frac{\partial \epsilon}{\partial x} = 0$

$x = L$: $\frac{\partial u}{\partial x} = 0, \frac{\partial v}{\partial x} = 0, \frac{\partial w}{\partial x} = 0, \frac{\partial k}{\partial x} = 0, \frac{\partial \epsilon}{\partial x} = 0$

$y = 0$: $u = 0, v = 0, w = 0, k = 0, \epsilon = \frac{1}{Re} \frac{\partial^2 k}{\partial y^2}$

$y = H$: $u = 0, v = v(x,H,z), w = 0, k = k(x,H,z), \epsilon = \epsilon(x,H,z)$

$z = 0$: $\frac{\partial u}{\partial z} = 0, \frac{\partial v}{\partial z} = 0, w = 0, \frac{\partial k}{\partial z} = 0, \frac{\partial \epsilon}{\partial z} = 0$

$z = W$: $\frac{\partial u}{\partial z} = 0, \frac{\partial v}{\partial z} = 0, \frac{\partial w}{\partial z} = 0, \frac{\partial k}{\partial z} = 0, \frac{\partial \epsilon}{\partial z} = 0$

(c) y-component-of-velocity profiles for x = 0

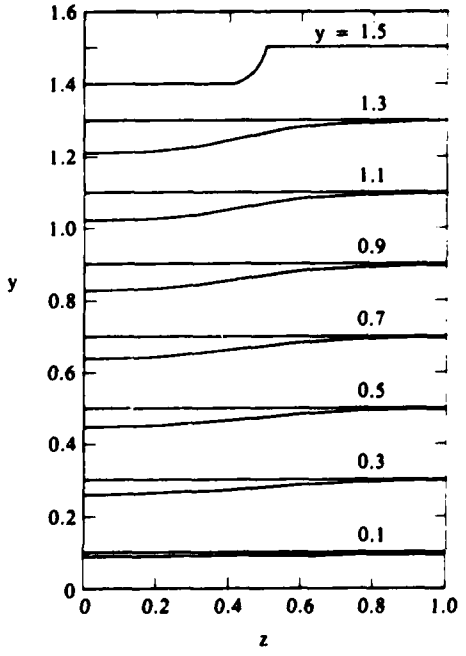

(d) Ground-plane pressure variation for x = 0

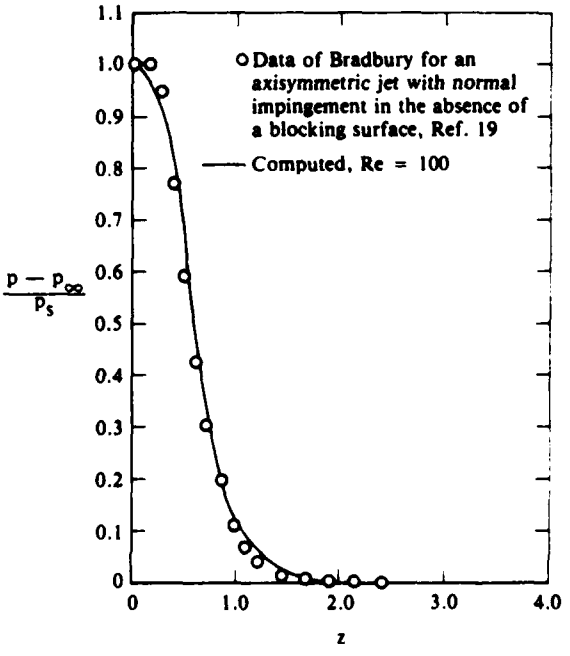

GP21-0078-10

Figure 10. Flow properties for an isolated jet with normal impingement in the presence of a blocking plate.

The boundary conditions for the velocity and turbulence quantities are defined in Figure 10(a). The entering jet velocity profile at the opening in the top plate is specified according to the following relation:

$$v(x, H, z) = -1.0 \qquad r < r_e \tag{119}$$

$$v(x, H, z) = \frac{(r - r_e)^2 - (r_e - r_b)^2}{(r_e - r_b)^2} \qquad r_e \leq r \leq r_b \,, \tag{120}$$

where $r = (x^2 + z^2)^{1/2}$, $r_b = 0.5$, and r_e was chosen to be 0.4 in the present calculations. For $r > 0.5$, $v(x, H, z) = 0$; u and w are zero along the entire upper surface of the computational domain. Within the entering jet, k and ε are computed using Equations (107) and (108); outside the jet along the upper plate, the turbulent kinetic energy vanishes, and the dissipation is computed from the wall form of the k transport equation,

$$\varepsilon = \frac{1}{Re} \frac{\partial^2 k}{\partial y^2} \,. \tag{121}$$

Symmetry conditions are applied on the planes $x = 0$ and $z = 0$, and the derivatives of all flow properties with respect to the coordinate normal to the surface are set equal to zero on the outflow planes $x = L$ and $z = W$. On the impingement surface, the three velocity components and the turbulent kinetic energy are set to zero, and the dissipation is evaluated using Equation (121).

The flowfield was calculated for the three-dimensional impinging jet in the presence of a blocking plate with Re = 100 and using 17 grid points in each coordinate direction. A streamline pattern for this configuration given in the computational (not physical) solution domain is shown in Figure 10(b), where pathlines are traced from the boundary of the entering jet. The profiles of the y component of velocity on the symmetry plane $x = 0$ are given in Figure 10(c) and illustrate the decay of the jet velocity as the ground is approached. The computed ground-plane pressure on the line $x = 0$ is shown in Figure 10(d) along with the data of Bradbury, Reference 19, for the normal impingement of an axisymmetric jet in the absence of a blocking surface.

4.3 Turbulent Interacting Jet-Impingement Flow

The jet-impingement flow of primary interest in the present study consists of two jets impinging perpendicular to the ground, creating opposing wall jets that collide to form a fountain upwash, as illustrated in Figure 1(b). Computations were made for this configuration with jets of equal and unequal initial diameters discharging through a blocking plate. The flowfield is established with specification of the nozzle height above ground, the centerline spacing, the diameter ratio, the velocity and turbulence profiles at the nozzle exit plane, and the Reynolds number based on the nozzle exit conditions.

When the jets are of equal diameter and equal strength, the flowfield is symmetrical with respect to the midplane of the fountain, and only half of the flow need be computed. The computational domain and the associated boundary conditions used in this case are the same as those shown in Figure 10(a) with $L = S/2$ and the boundary condition $\partial u/\partial x = 0$ for $x = L$ replaced by $u = 0$. The entering jet velocity profile is given by Equations (119) and (120).

However, the coordinate transformation in the x direction used for this geometry is modified from that used for the isolated jet to provide the proper grid resolution in the vicinity of the fountain symmetry plane. The following transformation is used:

$$\bar{x} = \frac{Ax}{Bx + C}, \qquad 0 \leq \bar{x} \leq S_{c1} \tag{122}$$

$$\bar{x} = S_{c1} + S_{c2} - \frac{D(S_{p1} + S_{p2} - x)}{E(S_{p1} + S_{p2} - x) + F}, \qquad S_{c1} \leq \bar{x} \leq S_{c1} + S_{c2}, \tag{123}$$

where

$$A = \frac{S_{c1}S_{p2}(S_{c1} + S_{c2})}{S_{c2}S_{p1}(S_{p1} + S_{p2})} \tag{124}$$

$$B = \frac{S_{c1}S_{p2} - S_{c2}S_{p1}}{S_{c2}S_{p1}(S_{p1} + S_{p2})} \tag{125}$$

$$C = 1 \tag{126}$$

$$D = \frac{S_{c2}S_{p1}(S_{c1} + S_{c2})}{S_{c1}S_{p2}(S_{p1} + S_{p2})} \tag{127}$$

$$E = \frac{S_{c2}S_{p1} - S_{c1}S_{p2}}{S_{c1}S_{p2}(S_{p1} + S_{p2})} \tag{128}$$

$$F = 1 \ . \tag{129}$$

In Equations (122) through (129), $\bar{x} = S_{c1}$ denotes the point in the computational domain where a coordinate transformation of the form given by Equation (122) originating at $\bar{x} = 0$ is matched to a coordinate transformation of the same form originating at the fountain midplane ($\bar{x} = S_{c1} + S_{c2}$) and extending toward the junction point. The constants A through F are determined such that their values and first two derivatives of the two transformations are continuous at $\bar{x} = S_{c1}$. The line $\bar{x} = S_{c1}$ in the computational plane corresponds to the line $x = S_{p1}$ in the physical domain, and the line $\bar{x} = S_{c1} + S_{c2}$ in the computational domain corresponds to the line $x = S_{p1} + S_{p2}$ in the physical domain.

For a twin-jet configuration with a centerline spacing of 6 nozzle diameters, the following values were used in the transformation: $S_{c1} = 1.5$, $S_{c2} = 0.5$, $S_{p1} = 2.0$, and $S_{p2} = 1.0$. The values of x as a function of $\bar{x}$ are tabulated below:

$\bar{x}$	x	$\bar{x}$	x
0.	0.		
0.1	0.1017	1.1	1.3469
0.2	0.2069	1.2	1.5000
0.3	0.3158	1.3	1.6596
0.4	0.4286	1.4	1.8261
0.5	0.5454	1.5	2.0000
0.6	0.6667	1.6	2.1818
0.7	0.7924	1.7	2.3721
0.8	0.9231	1.8	2.5714
0.9	1.0588	1.9	2.7805
1.0	1.2000	2.0	3.0000

The coordinate transformation given by Equation (118) is used in the z direction; no transformation is used in the y direction. The dimensions of the physical domain are 3.0 x 3.0 x 5.0 in the x, y, and z directions, respectively, and the dimensions of the computational domain are 2.0 x 3.0 x 1.5.

The flowfield was computed for this configuration (S = 6 and H = 3), which is presented in planar view in Figure 11(a), with Re = 200 and 22 grid points in the x direction, 32 in the y direction, and 17 in the z direction. The jet centerline variations of the velocity and turbulent kinetic energy are illustrated in Figure 11(b), and contour plots of the x and y components of velocity are shown for the planes z = 0 and z = 0.5 in Figures 11(c) through 11(f). In these plots $x' = x - S/2$. The ground-plane pressure distribution along the line z = 0 is shown in Figure 12(a), where the computed profile has been reflected about the fountain symmetry plane and compared with the data of Jenkins and Hill, Reference 20, for the same configuration in the absence of a blocking plate. The calculations provide good correlation with data in the impingement zone where the pressure gradient is associated with the deflection of the jet by the ground plane and is not significantly influenced by viscous effects. However, in the fountain region, viscous effects determine the level of the pressure recovery. (In an inviscid analysis of the present problem, the pressure would be unity at the fountain midline $x' = 0$, $y = 0$ since it is a stagnation line.) For the relatively low Reynolds number in the calculations, diffusive effects are large and, as illustrated in Figure 12(b), the opposing wall jets rapidly lose momentum such that the computed pressure increase in the vicinity of the fountain is smaller than the measured increase given in Reference 20, which corresponds to a Reynolds number on the order of 100 000. Calculations were first made with Re = 100, and there was no appreciable ground-plane pressure increase in the fountain. This solution was taken to initiate the solution for Re = 200, and using the latter, a solution for Re = 300 was attempted; however, a convergent solution could not be achieved for the highest Reynolds number.

The flowfield for equal-strength jets with S/D = 12 and H/D = 4 was computed using the x-coordinate transformation given by Equations (122) and (123) with $S_{c1} = 2.2$, $S_{c2} = 0.8$, $S_{p1} = 4.0$, and $S_{p2} = 2.0$. The values of the transformed and physical coordinates are listed below.

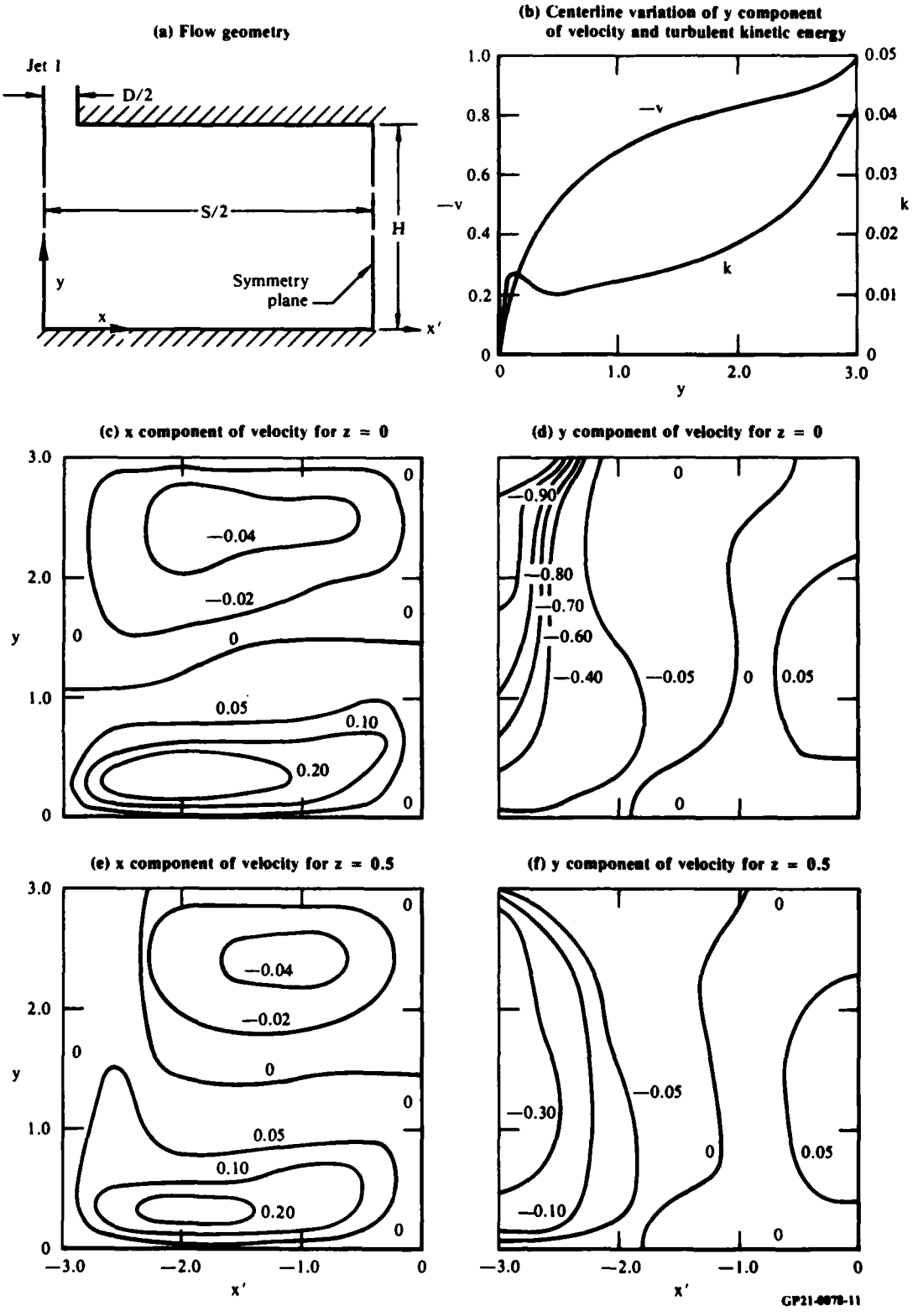

Figure 11. Flow properties for equal-strength jets with normal impingement (S/D = 6, H/D = 3, Re = 200).

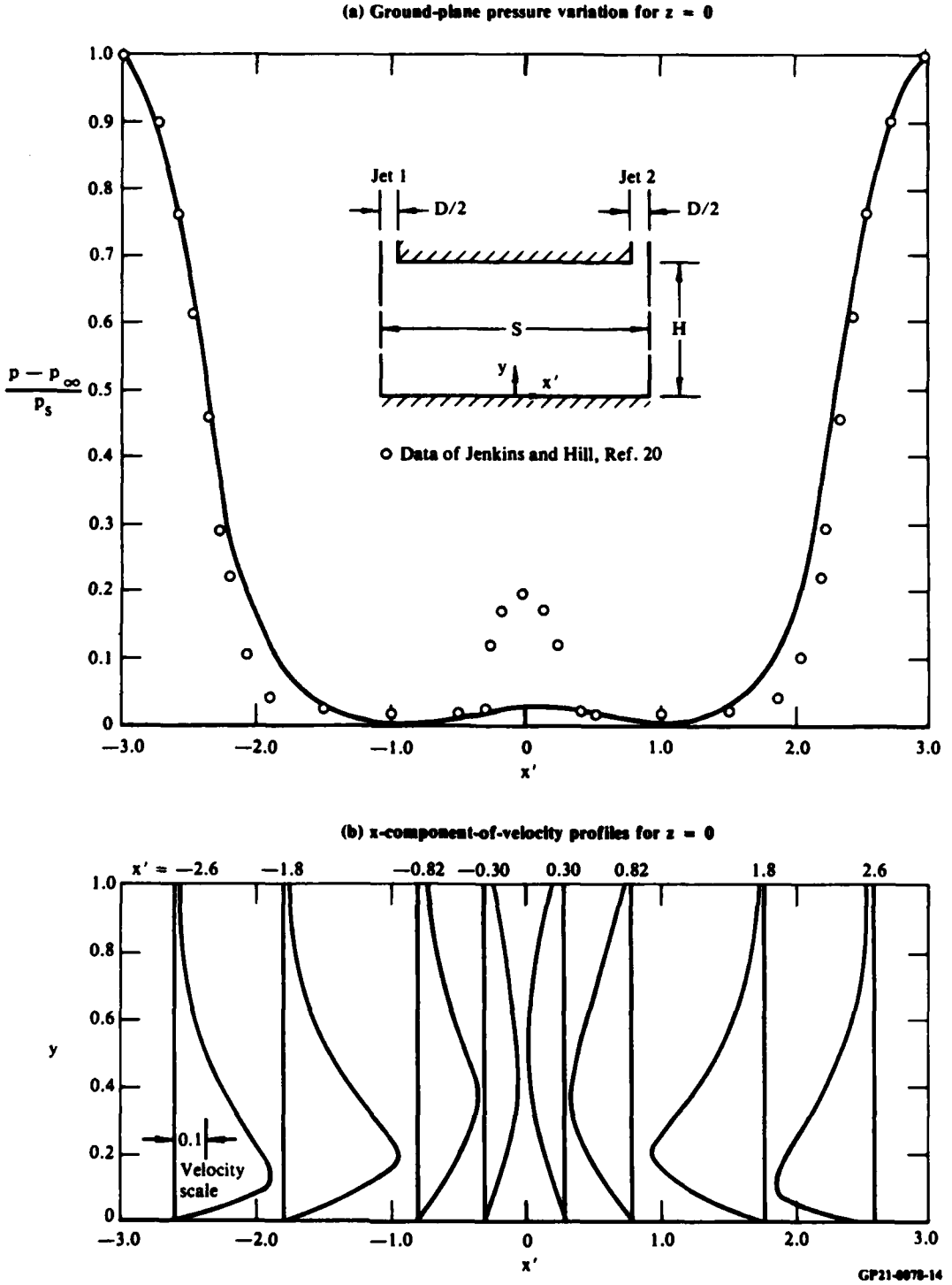

Figure 12. Flow properties for equal-strength jets with normal impingement (S/D = 6, H/D = 3, Re = 200).

$\bar{x}$	x	$\bar{x}$	x
0.	0.	1.6	2.7234
0.1	0.1468	1.7	2.9247
0.2	0.2963	1.8	3.1304
0.3	0.4486	1.9	3.3407
0.4	0.6038	2.0	3.5556
0.5	0.7619	2.1	3.7753
0.6	0.9231	2.2	4.0000
0.7	1.0874	2.3	4.2299
0.8	1.2549	2.4	4.4651
0.9	1.4257	2.5	4.7059
1.0	1.6000	2.6	4.9524
1.1	1.7778	2.7	5.2048
1.2	1.9592	2.8	5.4634
1.3	2.1443	2.9	5.7284
1.4	2.3333	3.0	6.0000
1.5	2.5263		

As in the previous case, the coordinate transformation given in Equation (118) is used for z, and no transformation is used for y. The dimensions of the physical domain in the x, y, and z directions, respectively, are 6.0 x 4.0 x 5.0, and the dimensions of the computational domain are 3.0 x 4.0 x 1.5 with 32, 42, and 17 nodes taken to establish the finite-difference grid. The flowfield was calculated for this case with Re = 100, and the ground-plane pressure distribution and x-component-of-velocity profiles for z = 0 are shown in Figures 13(a) and (b).

When the primary jets are of unequal diameter and unequal strength as they discharge through the blocking surface, the computational domain used to calculate the flowfield is shown in Figure 14. It is bounded by the three jet symmetry planes (x = 0, x = S, and z = 0), the outflow plane (z = W), and the two solid surfaces (y = 0 and y = H). For each of the jets, the entering velocity profile is evaluated using Equations (119) and (120).

The coordinate transformation defined by Equations (122) through (129) is used in the region $0 \leq x \leq S/2$ ($S_{c1} = 1.5$, $S_{c2} = 0.5$, $S_{p1} = 2.0$, and $S_{p2} = 1.0$) and is reflected about the midplane of the computational domain for $S/2 \leq x \leq S$. The values of x as a function of $\bar{x}$ are tabulated below.

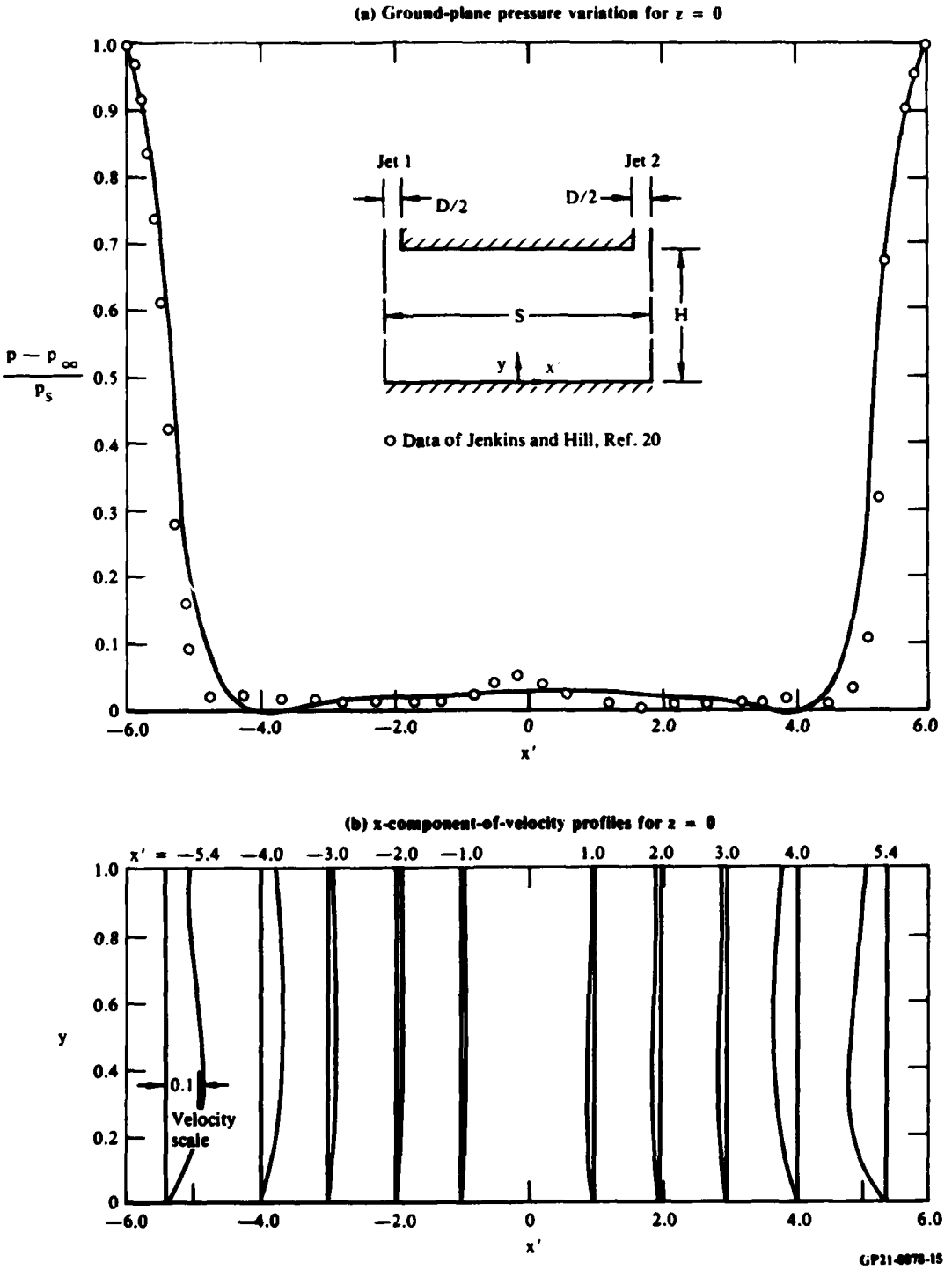

Figure 13. Flow properties for equal-strength jets with normal impingement (S/D = 12, H/D = 4, Re = 100).

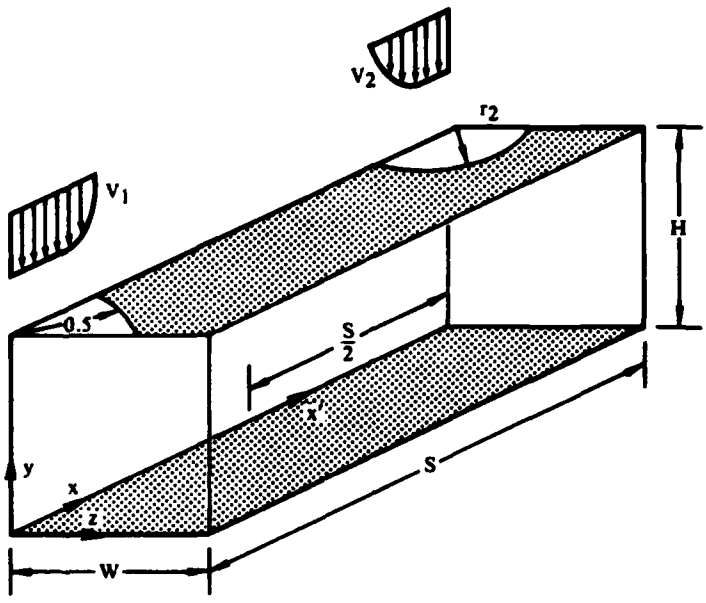

Boundary conditions

$x = 0$: $u = 0, \frac{\partial v}{\partial x} = 0, \frac{\partial w}{\partial x} = 0, \frac{\partial k}{\partial x} = 0, \frac{\partial \epsilon}{\partial x} = 0$

$x = S$: $u = 0, \frac{\partial v}{\partial x} = 0, \frac{\partial w}{\partial x} = 0, \frac{\partial k}{\partial x} = 0, \frac{\partial \epsilon}{\partial x} = 0$

$y = 0$: $u = 0, v = 0, w = 0, k = 0, \epsilon = \frac{1}{Re} \frac{\partial^2 k}{\partial y^2}$

$y = H$: $u = 0, v = v(x, H, z), w = 0, k = k(x, H, z), \epsilon = \epsilon(x, H, z)$

$z = 0$: $\frac{\partial u}{\partial z} = 0, \frac{\partial v}{\partial z} = 0, w = 0, \frac{\partial k}{\partial z} = 0, \frac{\partial \epsilon}{\partial z} = 0$

$z = W$: $\frac{\partial u}{\partial z} = 0, \frac{\partial v}{\partial z} = 0, \frac{\partial w}{\partial z} = 0, \frac{\partial k}{\partial z} = 0, \frac{\partial \epsilon}{\partial z} = 0$

GP21-0078-12

Figure 14. Computational domain for unequal-strength jets with normal impingement in the presence of a blocking plate.

$\bar{x}$	x	$\bar{x}$	x
0.	0.	2.1	3.2195
0.1	0.1017	2.2	3.4286
0.2	0.2069	2.3	3.6279
0.3	0.3158	2.4	3.8182
0.4	0.4286	2.5	4.0000
0.5	0.5455	2.6	4.1739
0.6	0.6667	2.7	4.3404
0.7	0.7924	2.8	4.5000
0.8	0.9231	2.9	4.6531
0.9	1.0588	3.0	4.8000
1.0	1.2000	3.1	4.9412
1.1	1.3469	3.2	5.0769
1.2	1.5000	3.3	5.2075
1.3	1.6596	3.4	5.3333
1.4	1.8261	3.5	5.4545
1.5	2.0000	3.6	5.5714
1.6	2.1818	3.7	5.6842
1.7	2.3721	3.8	5.7931
1.8	2.5714	3.9	5.8983
1.9	2.7805	4.0	6.0000
2.0	3.0000		

The coordinate transformation given in Equation (118) is used in the z direction, and no transformation is used in the y direction. The dimensions of the computational domain are 4.0 x 2.0 x 1.5, with 42, 22, and 17 grid points used in the $\bar{x}$, $\bar{y}$, and $\bar{z}$ directions, respectively.

Two flowfields were calculated for the case of two unequal-diameter jets with normal impingement. In both cases $S/D_1 = 6$, $H/D_1 = 2$, and $Re = 100$, where the Reynolds number is based on the exit-plane properties of jet 1. In the first configuration $d_2/d_1 = 0.75$ (with $r_{e1} = 0.4$, $r_{b1} = 0.5$, $r_{e2} = 0.3$, and $r_{b2} = 0.375$ in the entering jet velocity profiles), and in the second configuration $d_2/d_1 = 0.515$ ($r_{e1} = 0.4$, $r_{b1} = 0.5$, $r_{e2} = 0.206$, and $r_{b2} = 0.2575$). The ground-plane pressure profiles and x-component-of-velocity profiles for $z = 0$ are shown for these two cases in Figures 15 and 16, along with the pressure data measured by Jenkins and Hill, Reference 20, for the same configuration in the absence of a blocking plate with a Reynolds number on the order of 100 000. Again, the flowfield model provides the observed pressure distribution in the impingement zones but fails to provide the measured pressure variation in the fountain because of the diffusion effects for $Re = 100$.

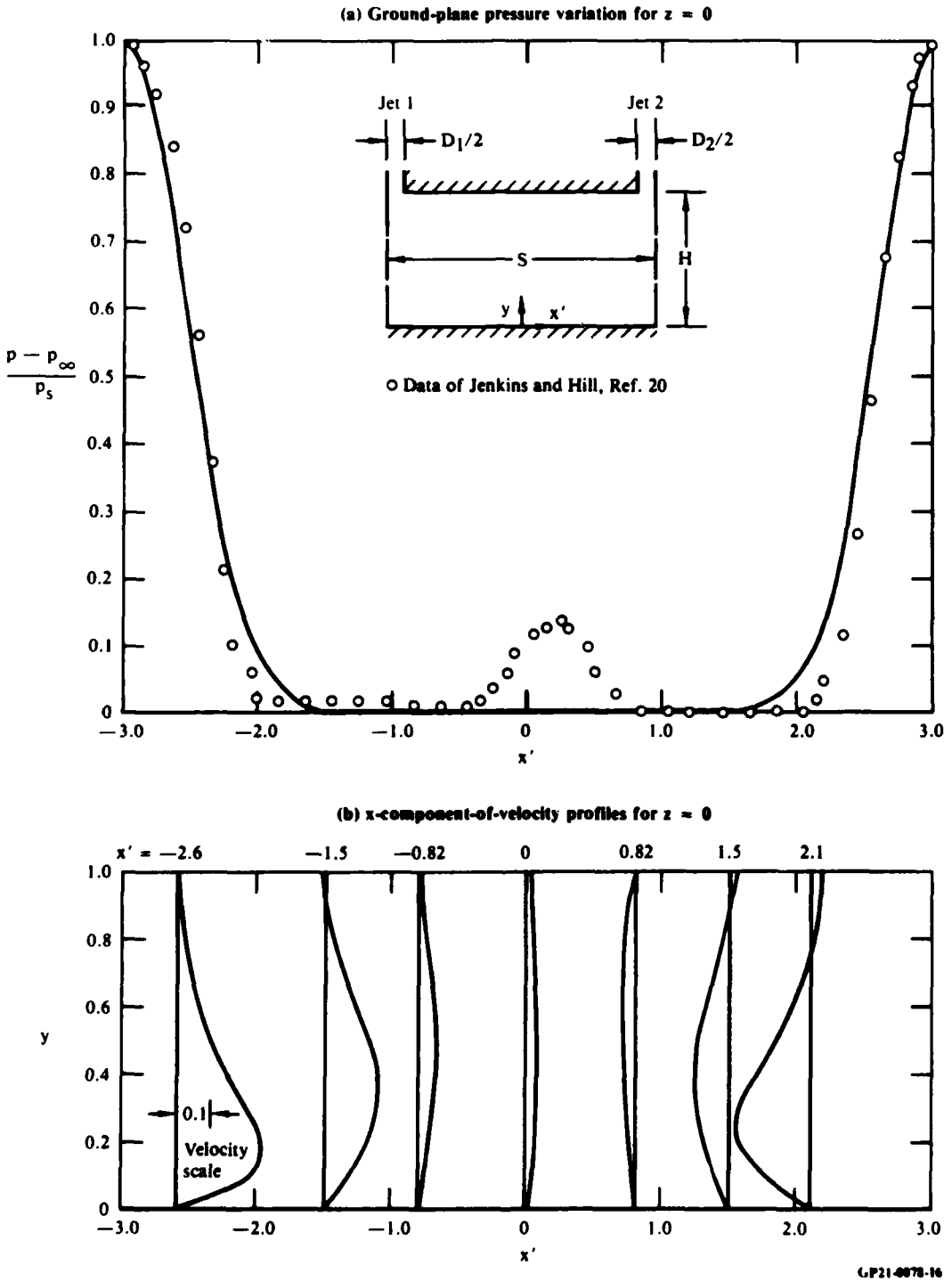

Figure 15. Flow properties for unequal-strength jets with normal impingement (S/D = 6, H/D = 3, D_2/D_1 = 0.75, Re = 100).

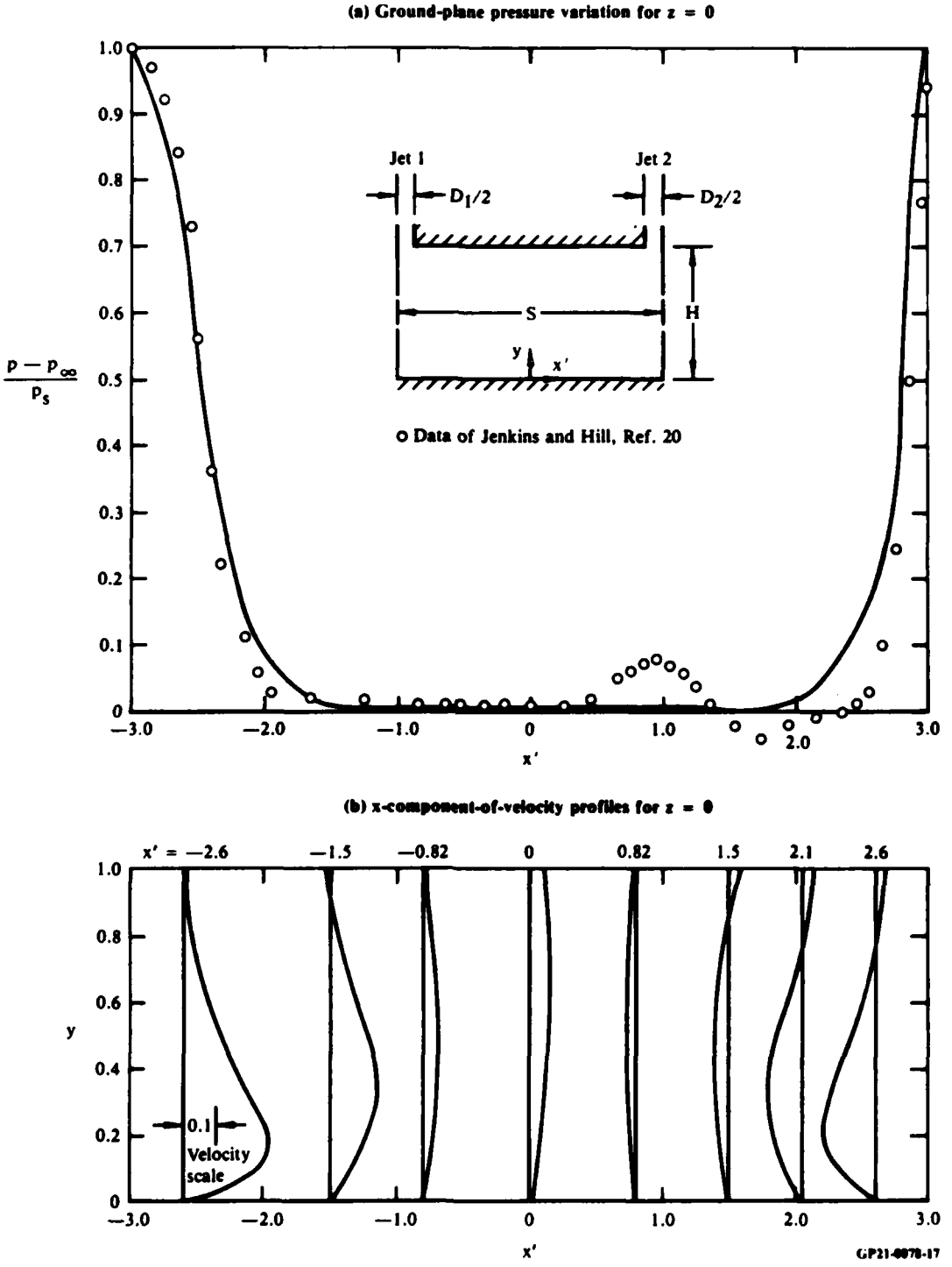

Figure 16. Flow properties for unequal-strength jets with normal impingement ($S/D_1 = 6$, $H/D_1 = 3$, $D_2/D_1 = 0.515$, Re = 100).

5. SUMMARY

Using the complete elliptic conservation equations for incompressible, steady, three-dimensional, viscous flow, a flowfield model has been solved numerically for isolated impinging jets and for two interacting impinging jets with fountain formation. The time-averaged Navier-Stokes and turbulence model equations were written in terms of Poisson equations for the velocity components and transport equations for the vorticity components, turbulent kinetic energy, and turbulent dissipation. Coordinate transformations were introduced into the system to extend the physical solution domain in the far field where relatively simple constraints could be imposed on the flow variables as boundary conditions. The Poisson equations were discretized using the conventional central-difference algorithm, and the transport equations were discretized using Agarwal's third-order-accurate upwind-difference scheme. The finite-difference forms of the Poisson equations were solved with the tridiagonal algorithm, and the finite-difference forms of the transport-type equations were solved with a pentadiagonal matrix-inversion routine. Alternating-direction line iteration was used to update the variables. Three-dimensional flowfields were computed for laminar channel flow (a test-case problem); isolated, turbulent, impinging jets with normal and inclined impingement; and interacting, turbulent, impinging jets with fountain formation.

Based on these computations, the following conclusions are made with regard to the flowfield model and the solution scheme used in the present work:

(1) Solution of the time-averaged Navier-Stokes equations in terms of velocity and vorticity is more efficient than solution of the equations in terms of scalar and vector potential functions and vorticity used in the previous jet-impingement work, Reference 8.

(2) The Jones-Launder two-equation turbulence model provides a better description of the turbulence field than the Glushko one-equation model used in the previous jet-impingement work, Reference 8, since the turbulence length-scale distribution need not be specified throughout the flowfield but rather is computed as part of the solution.

(3) The coordinate transformations used to specify the far-field boundary conditions provide a more general solution scheme since they eliminate the need to define the boundary conditions in the near field on the basis of empirical data, as was required in the previous jet-impingement work, Reference 8.

(4) Agarwal's third-order-accurate upwind-difference scheme used to discretize the transport-type equations requires less computing time and storage than Hoffman's augmented-central-difference scheme which was used to calculate the impinging jets described in Reference 8.

(5) The use of coarse finite-difference grids imposed by computer storage constraints limits the Reynolds number for which convergent solutions of the governing equations can be achieved. The surface pressure distribution computed for Re = 100 compares well with measurements obtained at higher Reynolds numbers in the impingement region for both isolated and interacting jets. However, in the latter case the solutions for a Reynolds number on the order of 100 do not provide the measured pressure increase in the fountain for a Reynolds number on the order of 100 000 because of the relatively large diffusion effects in the low-Reynolds-number results.

A potential approach for extending the present Navier-Stokes procedure to higher Reynolds numbers within the storage constraints of a CDC 7600 computer is to employ wall functions in the calculations. In the impinging-jet work completed to date at MDRL, the governing equations have been integrated to the wall through regions of steep velocity gradients using damping functions in the turbulence model to provide the proper low-Reynolds-number behavior near the solid surface. For Reynolds numbers on the order of 10^5, this approach would require an extremely fine finite-difference mesh near the solid boundaries, with an associated penalty in increased computing time as well as in increased storage. Using wall functions, which are described in Reference 21 for two-dimensional flows, the solutions of the time-averaged Navier-Stokes equations and high-Reynolds-number form of the Jones-Launder turbulence model equations are patched onto fully turbulent, local equilibrium wall-law profiles. With this method, damping functions are not required in the turbulence model, and the governing equations need not be integrated all the way to the

wall. The chief merit of this approach is that it economizes computer storage and time because it eliminates the need for a fine finite-difference mesh near the solid surface. The additional points that would be required near the solid boundaries without the use of wall functions can be distributed elsewhere in the flowfield.

Although application of the time-averaged Navier-Stokes and turbulence model equations to three-dimensional impinging jets is a complex computational problem, the present work has demonstrated reasonable agreement between the calculated and experimental flow properties. The disparities between the computations and measurements are not due to a deficiency in the flowfield model but rather to the Reynolds-number limitations imposed by the storage capacity of the CDC 7600 computer. No alternate computational method that does not rely on extensive empirical data has been reported to date that can treat the three-dimensional, interacting impinging jets as accurately as the method described in the present work.

REFERENCES

1. A. Rubel, Computations of Jet Impingement on a Flat Surface, AIAA J. 18, 168 (1980).
2. A. Rubel, Computations of the Oblique Impingement of Inviscid, Rotational Round Jets Upon a Plane Wall, AIAA Paper No. 80-1331, AIAA 13th Fluid and Plasma Dynamics Conference, July 1980.
3. R. K. Agarwal and W. W. Bower, Navier-Stokes Computations of Compressible, 2-D Impinging Jet Flowfields Using a Two-Equation Turbulence Model, AIAA Paper No. 80-0007, AIAA 18th Aerospace Sciences Meeting, January 1980.
4. D. R. Kotansky, N. A. Durando, D. R. Bristow, and P. W. Saunders, Multi-Jet Induced Forces and Moments on VTOL Aircraft Hovering In and Out of Ground Effect, Report No. NADC-77-229-30, Naval Air Development Center, 19 June 1977.
5. M. J. Siclari, W. G. Hill, Jr., and R. C. Jenkins, Investigation of Stagnation Line and Upwash Formation, AIAA Paper No. 77-615, AIAA/NASA Ames V/STOL Conference, June 1977.
6. K. R. Saripalli, Visualization of Multi-Jet Impingement Flow, AIAA Paper No. 81-1364, AIAA/SAE/ASME 17th Joint Propulsion Conference, July 1981.
7. M. J. Siclari, W. G. Hill, Jr., R. C. Jenkins, and D. Migdal, VTOL In-Ground Effect Flows for Closely Spaced Jets, AIAA Paper No. 80-1880, AIAA Aircraft Systems Meeting, August 1980.
8. W. W. Bower and G. R. Peters, Viscous Flowfields Induced by Three-Dimensional Lift Jets in Ground Effect, Report No. ONR-CR215-246-4F, Office of Naval Research, 1 July 1980.
9. W. P. Jones and B. E. Launder, The Prediction of Laminarization with a Two-Equation Model of Turbulence, Int. J. Heat and Mass Transfer 15, 301 (1972).
10. A. R. Mitchell, Computational Methods in Partial Differential Equations, (John Wiley and Sons Ltd., London, 1969).
11. R. K. Agarwal, A Third-Order-Accurate Upwind Scheme for Navier-Stokes Solutions at High Reynolds Numbers, AIAA Paper No. 81-0112, AIAA 19th Aerospace Sciences Meeting, January 1981.

12. R. K. Agarwal, A Third-Order-Accurate Upwind Scheme for Navier-Stokes Solutions in Three Dimensions, Computers in Flow Predictions and Fluid Dynamics Experiments, Proceedings of the Winter Annual Meeting of The American Society of Mechanical Engineers, November 1981.

13. Guide to Mathematical and Statistical Software Available at MCAUTO, McDonnell Douglas Automation Company, St. Louis, 1982.

14. L. C. Woods, A Note on the Numerical Solution of Fourth-Order Differential Equations, Aeronautics Quar. 5, 176 (1954).

15. R. J. Goldstein and D. K. Kreid, Measurement of Laminar Flow Development in a Square Duct Using a Laser-Doppler Flowmeter, J. Appl. Mech. 34, 813 (1967).

16. F. Giralt, C.-J. Chia, and O. Trass, Characterization of the Impingement Region in an Axisymmetric Turbulent Jet, Ind. Eng. Chem. Fundam. 16, 21 (1977).

17. R. S. Snedeker and C. duP. Donaldson, Experiments on the Oblique Impingement of Underexpanded Jets on a Flat Plate, A.R.A.P. Report No. 64, Princeton, N. J., April 1965.

18. M. T. Scholtz and O. Trass, Mass Transfer in a Nonuniform Impinging Jet, AIChE J. 16, 82 (1970).

19. L. J. S. Bradbury, The Impact of an Axisymmetric Jet onto a Normal Ground, Aeronautical Quart. 23, 141 (1972).

20. R. C. Jenkins and W. G. Hill, Jr., Investigation of VTOL Upwash Flows Formed by Two Impinging Jets, Grumman Research Department Report RE-548, November 1977.

21. B. E. Launder and D. B. Spalding, The Numerical Computation of Turbulent Flows, Computer Methods in Applied Mechanics and Engineering 3, 269 (1974).

DISTRIBUTION LIST

Addressees	Copies
Defense Technical Information Center Cameron Station Alexandria, VA 22314	12
Professor Bruce Johnson U.S. Naval Academy Engineering Department Annapolis, MD 21402	1
Library U.S. Naval Academy Annapolis, MD 21402	1
Technical Library David W. Taylor Naval Ship Research & Development Center Annapolis Laboratory Annapolis, MD 21402	1
Professor C. -S. Yih The University of Michigan Department of Engineering Mechanics Ann Arbor, MI 48109	1
Professor T. Francis Ogilvie The University of Michigan Department of Naval Architecture & Marine Engineering Ann Arbor, MI 48109	1
Office of Naval Research Code 200B 800 N. Quincy Street Arlington, VA 22217	1
Office of Naval Research Code 438 800 N. Quincy Street Arlington, VA 22217	3
NASA Scientific & Technical Information Facility P.O. Box 8757 Baltimore/Washington International Airport Maryland 21240	1
Professor Paul M. Naghdi University of California Department of Mechanical Engineering Berkeley, CA 94720	1
Librarian University of California Department of Naval Architecture Berkeley, CA 94720	1
Professor John V. Wehausen University of California Department of Naval Architecture Berkeley, CA 94720	1
Library David W. Taylor Naval Ship Research & Development Center Code 522.1 Bethesda, MD 20084	1
Mr. Justin H. McCarthy, Jr. David W. Taylor Naval Ship Research & Development Center Code 1552 Bethesda, MD 20084	1
Dr. William B. Morgan David W. Taylor Naval Ship Research & Development Center Code 1540 Bethesda, MD 20084	1
Director Office of Naval Research Eastern/ Central Regional Office Building 114, Section D 666 Summer Street Boston, MA 02210	1

DISTRIBUTION LIST
(continued)

Addressees	Copies	Addressees	Copies
Office of Naval Research Code 473 800 N. Quincy Street Arlington, VA 22217	1	The Society of Naval Architects and Marine Engineers One World Trade Center, Suite 1369 New York, NY 10048	1
Library Naval Weapons Center China Lake, CA 93555	1	Technical Library Naval Coastal System Laboratory Panama City, FL 32401	1
Technical Library Naval Surface Weapons Center Dahlgren Laboratory Dahlgren, VA 22418	1	Professor Theodore Y. Wu California Institute of Technology Engineering Science Department Pasadena, CA 91125	1
Technical Documents Center Army Mobility Equipment Research Center Building 315 Fort Belvoir, VA 22060	1	Director Office of Naval Research Western Regional Office 1030 E. Green Street Pasadena, CA 91101	1
Technical Library Webb Institute of Naval Architecture Glen Cove, NY 11542	1	Technical Library Naval Ship Engineering Center Philadelphia Division Philadelphia, PA 19112	1
Dr. J. P. Breslin Stevens Institute of Technology Davidson Laboratory Castle Point Station Hoboken, NJ 07030	1	Army Research Office P.O. Box 12211 Research Triangle Park, NC 27709	1
Professor Louis Landweber The University of Iowa Institute of Hydraulic Research Iowa City, IA 52242	1	Editor Applied Mechanics Review Southwest Research Institute 8500 Culebra Road San Antonio, TX 78206	1
R. E. Gibson Library The Johns Hopkins University Applied Physics Laboratory Johns Hopkins Road Laurel, MD 20810	1	Technical Library Naval Ocean Systems Center San Diego, CA 92152	1
Lorenz G. Straub Library University of Minnesota St. Anthony Falls Hydraulic Laboratory Minneapolis, MN 55414	1	ONR Scientific Liaison Group American Embassy - Room A-407 APO San Francisco 96503	1

DISTRIBUTION LIST
(continued)

Addressees	Copies
Library Naval Postgraduate School Monterey, CA 93940	1
Technical Library Naval Underwater Systems Center Newport, RI 02840	1
Engineering Societies Library 345 East 47th Street New York, NY 10017	1
Mr. Stanley W. Doroff Mechanical Technology, Inc. 2731 Prosperity Avenue Fairfax, VA 22031	1
Dr. Charles Watkins Head, Mechanical Engineering Department Howard University Washington, DC 20059	1
Professor S. M. Yen Coordinated Science Lab University of Illinois Urbana, IL 61801	1
Dr. G. Kulin National Bureau of Standards Mechanics Section Washington, DC 20234	1
Library Naval Sea Systems Command Code 09GS Washington, DC 20362	1
Maritime Administration Division of Naval Architecture 14th & E Streets, NW Washington, DC 20230	1
Librarian Naval Surface Weapons Center White Oak Laboratory Silver Spring, MD 20910	1
Defense Research and Development Attache Australian Embassy 1601 Massachusetts Avenue, NW Washington, DC 20036	1
Librarian Station 5-2 Coast Guard Headquarters NASSIF Building 400 Seventh Street, SW Washington, DC 20591	1
Library of Congress Science and Technology Division Washington, DC 20540	1
Dr. A. L. Slafkosky Scientific Advisor Commandant of the Marine Corps Code AX Washington, DC 20380	1
Maritime Administration Office of Maritime Technology 14th & E Streets, NW Washington, DC 20230	1
Naval Research Laboratory Code 2627 Washington, DC 20375	6
Mr. Thomas E. Peirce Naval Sea Systems Command Code 03512 Washington, DC 20362	1